An Evaluation of Several Low-Re Turbulence Models
Part 1- Flat-Plate Boundary Layer and Axisymmetric Separating Flows

M. I. Yaras
A.D. Grosvenor

Department of Mechanical and Aerospace Engineering
Carleton University, Ottawa, Ontario, CANADA K1S 5B6

Keywords: *turbulence modeling, diffusers, separated flows, wall-jet vortex generators*

Abstract

This two-part paper systematically examines several turbulence models in the context of a series of flows ranging from a simple flat-plate turbulent boundary layer to a three-dimensional vortical flow created by a wall jet. The test cases are chosen on the basis of availability of high-quality and detailed experimental data. All turbulence models are integrated to solid surfaces and consist of: Rodi's two-layer k-ε model, Chien's low-Reynolds number k-ε model, Wilcox's k-ω model, Menter's two-equation Shear-Stress-Transport model, and the one-equation model of Spalart and Allmaras. The objective of the study is to establish the prediction accuracy of these turbulence models with respect to two- and three-dimensional separated flows, and flows with high streamline curvature. At the same time, the study establishes the minimum spatial resolution requirements for each of these turbulence closures and identifies the proper low-Mach number preconditioning and artificial diffusion settings of a Reynolds-averaged Navier-Stokes algorithm for optimum rate of convergence and highest prediction accuracy. The first part of the paper describes the numerical algorithm, and presents results for a flat plate boundary layer and an axisymmetric separated flow. The second part contains simulations of the flow field associated with a wall-jet vortex generator.

Nomenclature

$a_1 \ldots a_4$: constants used in scaling the preconditioning parameter, c
a_s : a parameter used in outflow boundary treatment of pressure
c : parameter used in the preconditioning of Q in the $\partial Q / \partial t_p$ term
C_f : skin friction coefficient $(= \tau_w / (1/2 \rho_{ref} V_{ref}^2))$
C_p : static pressure coefficient
D : artificial dissipation operator; streamwise dimension of jet-exit hole
D_h : hydraulic diameter
D_j : jet diameter
$\mathcal{D}_k$: rate of destruction of turbulence kinetic energy
E, F, G : convective+diffusive flux vectors in the x, y and z directions, respectively
i, j, k : node indices in the ξ, η, ζ grid directions
K_c, K_d : constants used in determining the convective and diffusive pseudo-time-step limits
k : turbulence kinetic energy (m^2/s^2)
k^+ : turbulence kinetic energy normalized by U_τ^2
k_R^+ : wall-roughness height normalized by ν / U_τ
L : length of flat plate
n : direction normal to a wall
N_i, N_j, N_k : number of nodes in the i, j, and k grid

directions, respectively
P : pressure
P_{BC} : static pressure fixed at an outflow boundary
$\mathcal{P}_k$: rate of production of turbulence kinetic energy
Q : vector of conservation variables
r : radial co-ordinate
R_0 : hub radius in Driver and Johnston's annular-flow test section (=70mm)
R_s : radius of the streamline forming the "outer" boundary of the computational domain in Driver and Johnston's C.S0 test case
Re : Reynolds number
Re_θ : Reynolds number based on momentum thickness
S : surface area of control volume;
S_R : function used in obtaining wall value of ω in the k-ω model
t : time
t_p : pseudo time
U : x-velocity component
U_0 : inlet freestream velocity in Driver & Johnston's diffuser test section
U_τ : friction velocity (= $(\tau_w/\rho)^{1/2}$)
U^+ : streamwise velocity normalized by U_τ
V : velocity vector; y-velocity component
V_j : jet velocity
$\overline{V_j}$: space-averaged jet velocity
V_{local} : local velocity magnitude (m/s)
V_x : x-velocity component
V_y : y-velocity component
V_z : z-velocity component
VGJ : vortex-generator jet
VR : jet-to-crossflow velocity ratio
W : z-velocity component
x, y, z : cartesian co-ordinates
y_1 : perpendicular distance from wall to first grid node off the wall
$\kappa^{(2)},\kappa^{(4)}$: constants used in calculation of artificial dissipation
α_p : Coefficient used in outflow pressure specification
β_{wall} : coefficient used for ω_{wall} calculation in Menter's *SST* turbulence model
δ : boundary layer thickness
θ : vectored-jet skew angle from crossflow direction
Φ : vectored-jet-in-crossflow pitch angle from surface
λ : spectral radius of the inviscid flux Jacobian
ν : kinematic viscosity
ν_e : kinematic turbulence (eddy) viscosity
$\tilde{\nu}_e$: eddy-viscosity variable used in the Spalart-Allmaras turbulence model $= \nu_e(\chi^3 + 7.1^3)/\chi^3$
μ : dynamic viscosity
μ_e : dynamic eddy viscosity
χ : $\dfrac{\tilde{\nu}_e}{\nu}$
ρ : density
τ : viscous + Reynolds stress
τ_w : wall shear stress
Ω : magnitude of vorticity
ξ, η, ζ : co-ordinates aligned with grid directions on a structured grid
ε : dissipation rate of turbulence kinetic energy (m^2/s^3)
$\varepsilon^{(2)},\varepsilon^{(4)}$: scaling parameters used in calculation of artificial dissipation
$\tilde{\varepsilon}$: modified turbulence dissipation rate used in Chien's low-*Re* k-ε model
ω : specific dissipation rate of turbulence kinetic energy (1/s)
ϑ : size of control volume

Superscripts

ref : reference quantities used for nondimensionalization
wall : value on the wall

1 Introduction

Turbulence closures based on one or two partial differential transport equations exist in virtually every commercial general-purpose computational fluid dynamics (*CFD*) code today. These models are built on the eddy-viscosity hypothesis, and as such lack representation of turbulence anisotropy and Reynolds-stress relaxation in response to sudden changes in the strain field. Despite these shortcomings, however, they are still preferred over higher-order Reynolds stress closures in most instances due to their

substantially lower computational overhead. Traditionally, these eddy-viscosity models have relied on wall functions for boundary conditions at solid surfaces. These functions are based on the assumption of local equilibrium of turbulence, i.e. they assume the existence of a balance between the production and dissipation rates of turbulence. This assumption is often not valid, such as in unsteady flows, in separated boundary layers, or in instances where strong secondary flows penetrate into the viscous sublayer [1]. Significant increases in computational power over the last decade has made more refined resolution of the boundary layer practical. This, in turn, has allowed integration of the turbulence transport equations to solid surfaces, circumventing the restrictions brought about by the wall-function approach. Numerous "low Reynolds number" turbulence models have been developed that facilitate this process of integration to solid surfaces [2,3]. It has been suggested that as many as 60 to 100 nodes are needed across a boundary layer for proper numerical resolution with such turbulence models [4]. As more and more of these models are incorporated into mainstream computational tools, it is important that systematic studies be undertaken to establish their accuracy and minimum spatial-resolution requirements.

Five such turbulence models have been evaluated in the present study for prediction accuracy, numerical robustness and computational efficiency based on test cases ranging from a two-dimensional equilibrium boundary layer to a three-dimensional separated flow. These turbulence models consists of: the low-*Re* k-ε model of Chien [5], the two-layer k-ε model of Rodi and his co-workers [6], the k-ω model of Wilcox [7], the two-equation shear-stress-transport model of Menter [8], and the one-equation eddy-viscosity model of Spalart and Allmaras [9]. The simulations contained in this study are presented in the order of increasing flow complexity. The first flow consists of an equilibrium flat-plate turbulent boundary layer performed as a baseline test case. The second test case is based on an axisymmetric annular diffusing flow allowing evaluation of the turbulence models with respect to behavior under adverse streamwise pressure gradient and separated conditions. These test cases are then followed by a significantly more complex, three-dimensional flow associated with a vortex-generator jet, presented in Part-2 of this study.

2 Numerical Technique

2.1 Algorithm

A Navier-Stokes solver developed by the first author of this work has been used in the simulations. The algorithm is based on the solution of the Navier-Stokes equations expressed in integral, strong-conservation-law form:

$$\int_{\forall}(Q_t + E_x + F_y + G_z)d\forall = 0 \qquad (1)$$

where the subscripts indicate derivatives and,

$$Q = \begin{pmatrix} \rho \\ \rho V_x \\ \rho V_y \\ \rho V_z \end{pmatrix}, \quad E = \begin{pmatrix} \rho V_x \\ \rho V_x^2 + p - \tau_{xx} \\ \rho V_x V_y - \tau_{xy} \\ \rho V_x V_z - \tau_{xz} \end{pmatrix},$$

$$F = \begin{pmatrix} \rho V_y \\ \rho V_x V_y - \tau_{yx} \\ \rho V_y^2 + p - \tau_{yy} \\ \rho V_y V_z - \tau_{yz} \end{pmatrix}, \quad G = \begin{pmatrix} \rho V_z \\ \rho V_x V_z - \tau_{zx} \\ \rho V_y V_z - \tau_{zy} \\ \rho V_z^2 + p - \tau_{zz} \end{pmatrix} \qquad (2)$$

with

$$\tau_{xx} = \frac{2}{3}\rho(\nu+\nu_e)\left(2\frac{\partial V_x}{\partial x} - \frac{\partial V_y}{\partial y} - \frac{\partial V_z}{\partial z}\right),$$

$$\tau_{xy} = \rho(\nu+\nu_e)\left(\frac{\partial V_x}{\partial y} + \frac{\partial V_y}{\partial x}\right) \qquad (3)$$

and similarly for the remaining normal and shear stresses.

Although the algorithm has been developed for the prediction of both incompressible and compressible flows, the present description is given for incompressible flows in keeping with the nature of the present simulations. Discretization in space is based on a vertex-centered finite-volume scheme using a structured grid of quadrilateral (hexahedral in three-dimensional space) cells [10]. In this approach, the

conserved variables are stored at the vertices of the grid cells, and the faces of the control volume associated with a vertex are formed by connecting the centroids of the quadrilaterals surrounding the vertex to the midpoints of the edges passing through the vertex. Both convective and diffusive fluxes are calculated at the vertices and are interpolated to the control-volume faces. The spatial gradients appearing in the diffusive fluxes at a vertex are obtained by applying Gauss' divergence theorem to the control volume surrounding the vertex.

On a uniform grid, the interpolation of the flux terms outlined above is equivalent to centered differencing, yielding second-order accuracy. Except for very low grid-cell Reynolds numbers, such treatment of convective fluxes is well-known to cause instability and requires inclusion of an artificial dissipation term into the governing equations. This artificial dissipation term, $D(Q)$, is traditionally constructed from second- and fourth-order differences of the conservation variables in all grid directions [11], i.e.:

$$\int_{\vartheta}(Q_t + E_x + F_y + G_z)d\vartheta - (D_\xi^{(2)} - D_\xi^{(4)} + D_\eta^{(2)} - D_\eta^{(4)} + D_\zeta^{(2)} - D_\zeta^{(4)})Q = 0 \quad (4)$$

where subscripts ξ, η, ζ denote the three grid directions of the structured grid. For instance considering the ξ direction,

$$D_\xi^{(2)}Q = \nabla_\xi((\lambda_\xi)_{i-1/2,j,k}(\varepsilon_\xi)^{(2)}_{i-1/2,j,k})\Delta_\xi Q_{i,j,k} \quad (5)$$

$$D_\xi^{(4)}Q = \nabla_\xi((\lambda_\xi)_{i-1/2,j,k}(\varepsilon_\xi)^{(4)}_{i-1/2,j,k})\Delta_\xi\nabla_\xi\Delta_\xi Q_{i,j,k} \quad (6)$$

where i,j,k denote indices in the ξ, η, ζ grid directions, λ is the spectral radius of the inviscid-flux Jacobian, and ∇_ξ, Δ_ξ are first-order forward and backward differencing operators in the ξ grid direction. These operators need to be modified at computational domain boundaries, and the approach recommended by Swanson and Turkel [12] is adopted in the present algorithm. $\varepsilon^{(2)}$ and $\varepsilon^{(4)}$ are scaling parameters for the dissipation terms. $\varepsilon^{(2)}$ is assigned a value such that the $D^{(2)}$ term is activated only in regions of high pressure gradients:

$$(\varepsilon_\xi)^{(2)}_{i-1/2,j,k} = \kappa^{(2)}\max((\varphi_\xi)_{i-1,j,k}, (\varphi_\xi)_{i,j,k}) \quad (7)$$

$$(\varphi_\xi)_{i,j,k} = \left|\frac{\Delta_\xi\nabla_\xi p_{i,j,k}}{(4+\Delta_\xi\nabla_\xi)p_{i,j,k}}\right| \quad (8)$$

where $\kappa^{(2)}$ is set to 0.25. $\varepsilon^{(4)}$ is quantified using:

$$(\varepsilon_\xi)^{(4)}_{i-1/2,j,k} = \max(0, \kappa^{(4)} - (\varepsilon_\xi)^{(2)}_{i-1/2,j,k}) \ , \quad (9)$$

where $\kappa^{(4)}$ is a constant. In absence of high pressure gradients, only the third-order accurate $D^{(4)}$ term is activated, allowing the second order formal accuracy of the spatial discretization to be retained. Due to low levels of local pressure gradients in the simulations presented herein, only the $D^{(4)}$ term influenced the solution. The minimum value of $\kappa^{(4)}$ that allowed stable convergence will be presented in later sections.

The spectral radii of the inviscid flux Jacobian matrices are the common scaling parameters for the artificial dissipation terms. Matrix valued scaling [13] results in less artificial diffusion entering the numerical solution, albeit at the expense of reduced convergence rates [14]. In the present algorithm the scalar method of scaling is chosen. For example, the $(\lambda_\xi)_{i-1/2,j,k}$ component is obtained from:

$$(\lambda_\xi)_{i-1/2,j,k} = \left(|V_\xi S_\xi| + ((c/a_1)^2 + V_\xi^2)^{1/2}|S_\xi|\right)_{i-1/2,j,k} \quad (10)$$

where S_ξ is the control volume surface facing the ξ grid direction, and c/a_1 is a preconditioning parameter, to be described later.

Discretization of the temporal derivative, Q_t, appearing in Eqn.1 is based on three-point backward differencing, yielding second order accuracy in time. An exception is the first time increment which is based on a two-point scheme. At each real-time increment, the discretized governing equations are then solved iteratively using pseudo-time stepping for relaxation:

$$(Q_{t_p}\vartheta)_{i,j,k} + \int_{\vartheta_{i,j,k}}(Q_t + E_x + F_y + G_z)d\vartheta - D(Q_{i,j,k}) = 0 \quad (11)$$

For the steady-flow simulations presented herein, the temporal derivative, Q_t, was not included in the computations. The vector of conservation variables,

Q, used in the pseudo-time derivative, Q_{t_p}, is preconditioned to extend the range of applicability of the algorithm to low Mach-number flows..

The following form of preconditioning has been adopted which is similar to the one proposed by Turkel [15]:

$$\frac{\partial Q}{\partial t_p} = \begin{pmatrix} \left(\frac{a_1}{c}\right)^2 \frac{\partial p}{\partial t_p} \\ \left(\frac{a_2}{c}\right)^2 V_x \frac{\partial p}{\partial t_p} + \frac{\partial(\rho V_x)}{\partial t_p} \\ \left(\frac{a_3}{c}\right)^2 V_y \frac{\partial p}{\partial t_p} + \frac{\partial(\rho V_y)}{\partial t_p} \\ \left(\frac{a_4}{c}\right)^2 V_z \frac{\partial p}{\partial t_p} + \frac{\partial(\rho V_z)}{\partial t_p} \end{pmatrix} \qquad (12)$$

where a_1, a_2, a_3, a_4 are constants and c is a parameter, which was scaled on the local flow velocity for the present simulations. The same value was assigned to the constants $a_{i=1,4}$. Variations were observed for the optimum value of this constant amongst the test cases of the study.

The pseudo-time increments are adjusted locally to the maximum allowable value dictated by convective and diffusive numerical stability limitations:

$$\frac{1}{(\Delta t_p)_{i,j,k}} \geq \left(\frac{1}{\Delta t_c} + \frac{1}{\Delta t_d}\right)_{i,j,k} \qquad (13)$$

$$\left(\frac{1}{\Delta t_c} + \frac{1}{\Delta t_d}\right)_{i,j,k} = \left(\frac{\Sigma\lambda}{K_c \vartheta} + \frac{1}{K_d \vartheta^2}\Sigma(\nu+\nu_e)S^2\right)_{i,j,k} \qquad (14)$$

where the summations are performed over the surfaces of the control volume. The values for the constants K_c and K_d will be given later.

Marching in pseudo time is based on Runge-Kutta integration with explicit odd-numbered and implicit even-numbered stages. Such implicit treatment of alternate stages is analogous to the well-known implicit residual smoothing procedure [11], and enhances the stability margin of the algorithm over the purely explicit approach. A modified version of the Strongly-Implicit Procedure of Stone ([16], [17]) is used for the implicit stages. For computational efficiency, the artificial dissipation terms are evaluated only during the odd-numbered stages. For the simulations presented herein, two-stage Runge-Kutta integration was found to be sufficient to damp-out the high frequency pseudo-transients. The coefficients of both stages were set to 1.0.

Although the Runge-Kutta time integration process efficiently removes high-frequency errors during pseudo-time stepping, it is not efficient in coping with errors of relatively large wave lengths. A multigrid scheme is used to deal with the longer wave lengths. The scheme is based on Full-Approximation-Storage [18] utilizing V cycles with conservative area-weighted interpolation during restriction and linear interpolation during prolongation. For the present simulations, two levels of grids with two coarse-grid time increments per cycle was found to provide the best trade-off between rate of reduction of residuals and increased computational effort due to the prolongation and restriction operations over each multigrid cycle. Due to reduced spatial resolution on the coarse grid, the physical and artificial diffusion terms were calculated on the fine-grid level only.

2.2 Turbulence Models

The turbulence models evaluated in the present study are Rodi's two-layer k-ε model [6] , Chien's low-Reynolds number k-ε model [5], Wilcox's k-ω model [7], Menter's two-equation Shear-Stress-Transport model [8], and the one-equation model of Spalart and Allmaras [9]. These turbulence models were used in their standard configurations, with the various empirical constants set to values proposed by their respective developers (see reference [19] for details). As such, the models are not presented in detail here in the interest of brevity.

In the transport equations of turbulence, the discretization of the convective and diffusive terms, and the formulation of artificial dissipation is the same as for the mass and momentum equations described earlier. Point-implicit linearization of the source term is utilized for enhanced stability. The resultant

equations are solved with the remaining governing equations in a coupled fashion. Pre-conditioning of the pseudo-time derivative is not required for the turbulence equations, hence the constant a appearing in the pseudo-time derivative of the mass and momentum equations (see Eqn. 12) is set to zero for the transport equations of turbulence.

At wall boundaries, k, $\tilde{\varepsilon}$, $d\varepsilon/dn$ and $\tilde{\nu}_e$ are set to zero. In the *SST* turbulence model the wall value of ω is determined using:

$$\omega_{wall} = \frac{6\beta_{wall}\nu}{0.075 y_1^{\ 2}} \tag{15}$$

A value of β_{wall}=10 was given by Menter [8], whereas Hellsten [20] suggested 1.25. Sensitivity of the simulation results to the value of β_{wall} will be discussed in the context of flat-plate boundary layer simulations.

In the k-ω turbulence model the wall value of ω is obtained from:

$$\omega_{wall} = \frac{U_\tau^2 S_R}{\nu} \tag{16}$$

where,

$$S_R = \begin{cases} \left(50 / k_R^+\right)^2 & k_R^+ \le 25 \\ 100 / k_R^+ & k_R^+ > 25 \end{cases} \tag{17}$$

The parameter k_R^+ was calculated as per the recommendation of Hellsten [20] for smooth walls:

$$k_R^+ = 2.4 y_1^{+0.85} \tag{18}$$

3 Simulations of a Flat Plate Boundary Layer

The flat-plate turbulent boundary layer is expected to pose the least challenge to a turbulence model due to the equilibrium state of the turbulence. As such, the relatively complex turbulence models considered in this study are expected to perform well for this flow. The primary motivation for including this flow into the study was to establish the baseline performance of the models in question, and establish their sensitivity to spatial resolution, freestream turbulence settings and numerical diffusion.

3.1 Computational Domain, Boundary Conditions and Iteration Parameters

The simulations were conducted with a computational domain of 0.15m height, 2.1m length, freestream velocity of 33 m/s, and a Reynolds number based on length (L) of 4.5×10^6. A 0.1m long "slip wall" boundary was placed upstream of the plate leading edge. Both the upper and aft boundaries of the computational domain were set as outflow boundaries with a fixed, spatially uniform static pressure. All flow variables other than pressure were extrapolated to the outflow boundaries from within the computational domain. At the inflow boundary, uniform distributions of velocity, flow direction and turbulence properties were imposed, and static pressure was extrapolated from the interior nodes.

The inflow turbulence properties were set to: $k = 1.3\times10^{-3}$, $\varepsilon = 7$ for the k-ε models of Rodi and Chien; $k = 1.8\times10^{-6}$, $\omega = 100$ for the k-ω and *SST* models; and $\chi = 0.77$ for the *SA* model. The initial distributions of the turbulence parameters throughout the computational domain were matched to these values at the inflow boundary. Rodi's model was an exception to this, for it was observed that low initial values of k resulted in convergence towards laminar flow before arriving at the turbulent solution, which increased the required computing time. Use of an initial value of k= 0.11, corresponding to μ_e/μ= 10, avoided this particular transient path. During the course of pseudo-time marching to a steady state solution, it is plausible for the turbulence parameters to temporarily assume negative values. This nonphysical behavior would likely cause divergence of the solution. This problem was avoided by imposing lower limits on the turbulence parameters which, in the present case, were matched to the turbulence specifications at the inflow boundary. This choice of lower limits prevented decay of freestream turbulence with downstream distance, thereby providing homogeneous action of simulated freestream turbulence along the length of the boundary layer.

For optimum rate of convergence to a solution, the artificial compressibility parameter, c/a, was set to $max[1.0\text{m/s};1.4V_{local}]$. Acceptable levels of

convergence was feasible with values up to max[1.0m/s;2.2V_{local}]. Calculation of convective and diffusive pseudo-time-step limits were based on K_c=1.8 and K_d=0.5, and the artificial-diffusion parameter, κ_4 , was set to 0.005.

3.2 Computational Grid

The simulations were performed for several combinations of boundary layer cross-stream resolution and y_1^+ values to establish sensitivity to these parameters. The first grid consisted of 273 nodes in the streamwise direction with clustering towards the leading edge, and 129 nodes in the cross-stream direction with 82 of these nodes contained within the maximum boundary layer thickness of 0.04m at the trailing end of the plate. The node count within the boundary layer was determined on the basis of boundary layer edge location identified with an edge velocity that is 99% of the freestream value. The distance of the first node from the plate surface corresponded to y_1^+=1.25 at x/L=0.6. This was the finest grid tested and was chosen to suit the y_1^+ as well as boundary layer resolution requirements of all four models based on the information available in the literature [21,24,25]. Subsequent grids were reduced in resolution, and the distance of the first node from the wall was varied in an attempt to identify the coarsest grid with the largest y_1^+ that provided C_f values within 5% of the experimental data. The 5% threshold was chosen somewhat arbitrarily as a reasonable level of accuracy for C_f in design-cycle analysis. The streamwise number of nodes in these coarser grids was set to 97. Cross-stream resolution was reduced to 45 and 23 nodes, yielding 31 and 15 nodes, respectively, within the boundary layer thickness at the trailing end of the plate. The distance of the first node from the wall was varied within these two coarse grid resolutions. Values of approximately y_1^+=3 and y_1^+= 5 were established at x/L=0.6.

3.3 Simulation Results

In what follows, the predicted skin friction coefficient and the velocity profile at x/L=0.6 are compared with the data of Wieghardt and Tillmann [22], whereas the data compiled by Patel et al. [23] is used as a reference for the predicted k profile at the same streamwise position. The band of variation in the k data compiled by Patel *et al.* is as large as $\pm$25%. Thus, evaluation of predicted accuracy for k is qualitative. The choice of x/L=0.6 as the streamwise location for analysis of the results was arbitrary and represents the trends observed at other streamwise positions.

Predicted streamwise distribution of C_f and profiles of streamwise velocity and turbulence kinetic energy at x/L=0.6 are compared to experimental data in Figures 1 to 5. For the k-ω and *SST* turbulence models the results are shown for two of the grids only, since the discrepancy between the predicted and experimental C_f data was well beyond the 5% threshold with the remaining grids. In the plots, symbols are included to correspond with node locations on the prediction curves so as to provide a visual indication of the boundary layer resolution. Rodi's k-ε model displays the least amount of dependence on boundary-layer resolution and y_1^+, and is closely followed by the *SA* model. Both models produce reasonably accurate results for the C_f and velocity distributions on the coarsest grid considered (y_1^+=5 at x/L=0.6; 15 nodes in the boundary layer at x/L=1.0). The *SST* and k-ω models, on the other hand, already yield prediction errors on the second finest grid (y_1^+=2.8 at x/L=0.6; 31 nodes in the boundary layer at x/L=1.0) that are somewhat greater than those with the k-ε and *SA* models on the coarsest grid. These results were used as guidelines in the construction of the grids in near-wall regions of the remaining test cases of this study. Convergence problems were encountered with Chien's k-ε model, caused by excessive amounts of production of turbulence energy at the leading edge. Rather than limiting the production of turbulence, simulations with this model were based on a computational domain with an inflow positioned downstream of the leading edge of the plate. The inflow boundary-layer profiles of mean-flow and turbulence properties were obtained from the simulations with Rodi's k-ε model. For convergence, it was necessary to adjust the lower limit of c/a from 1.0m/s to 15.0m/s, and K_d from 0.1 to 0.5. As shown in Figure 5, the prediction accuracy is comparable to those of other models. The C_f trend in close vicinity of the inflow boundary is the result of

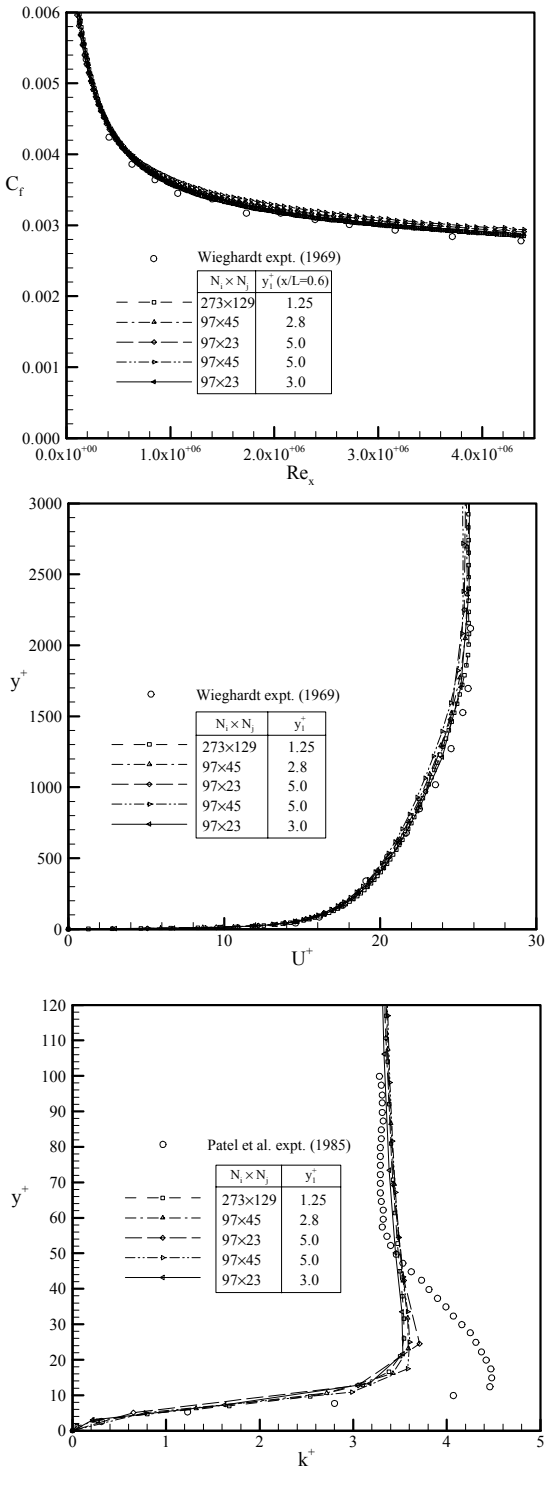

Figure 1. Flat-plate predictions based on Rodi's *k-ε* model - sensitivity to spatial resolution (velocity and *k* profiles correspond to *x/L*=0.6)

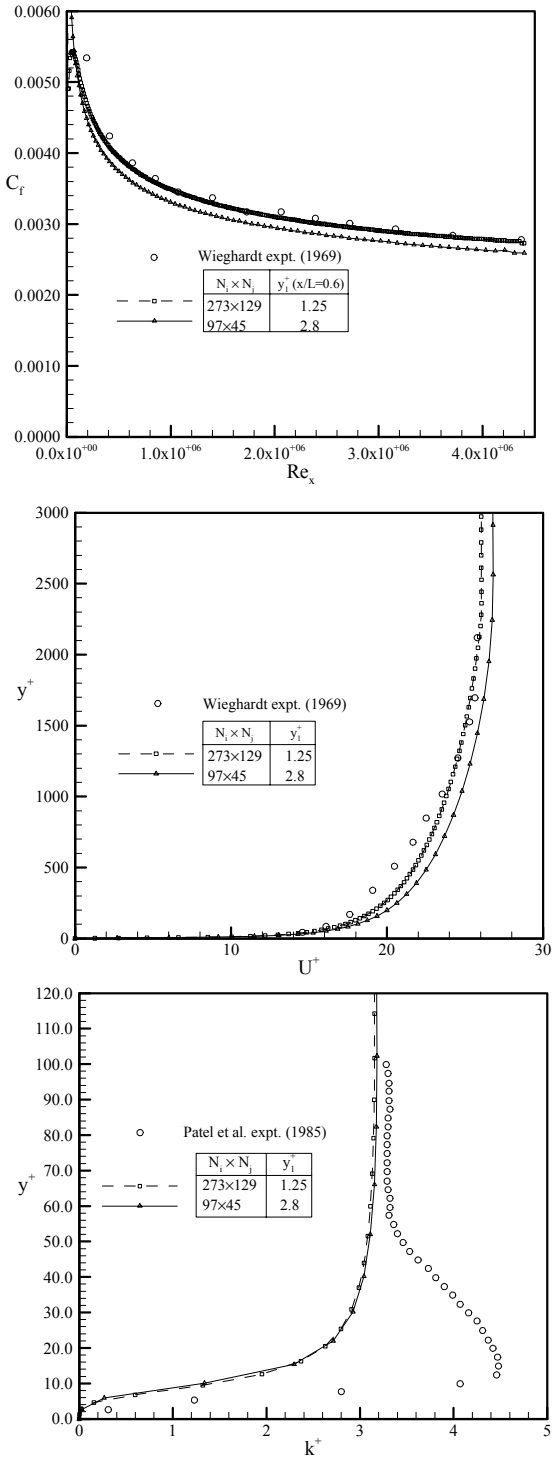

Figure 2. Flat-plate predictions based on the *k-ω* model - sensitivity to spatial resolution (velocity and *k* profiles correspond to *x/L*=0.6)

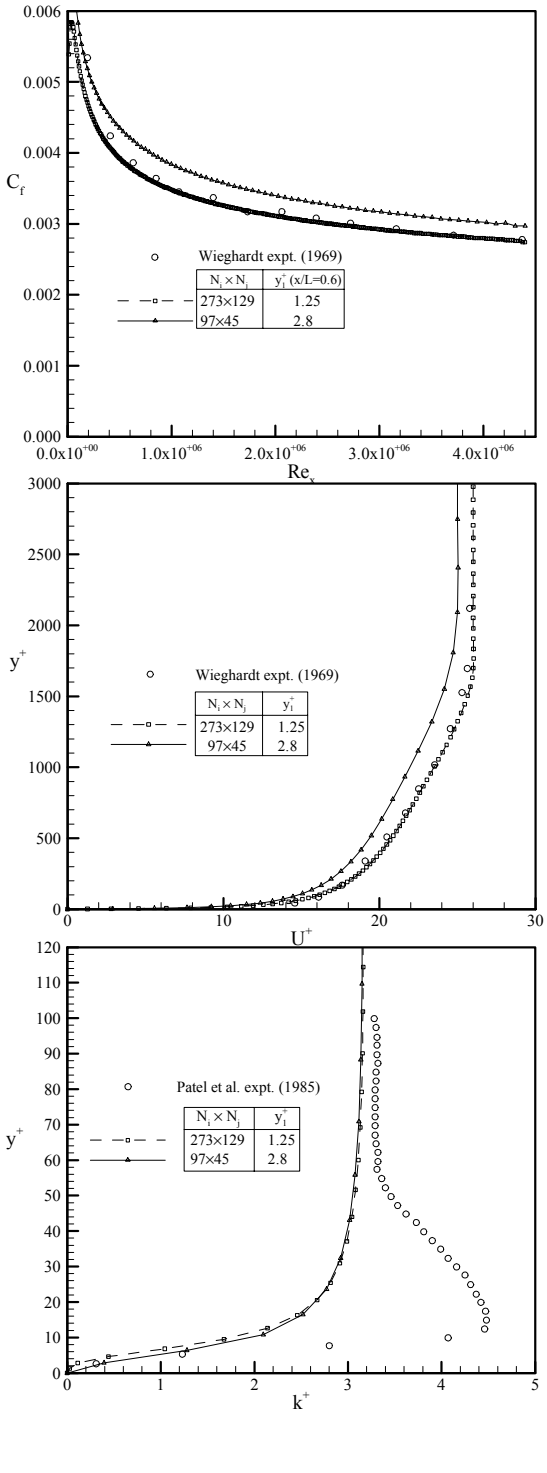

Figure 3. Flat-plate predictions based on Menter's *SST* model - sensitivity to spatial resolution (velocity and *k* profiles correspond to *x/L*=0.6)

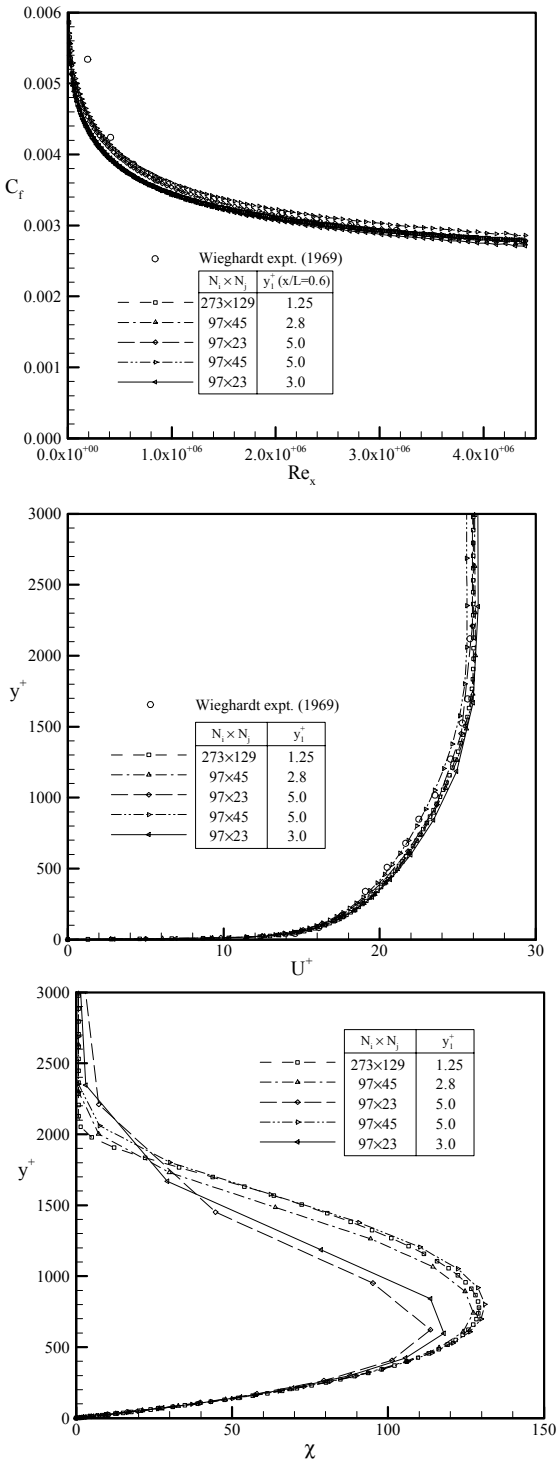

Figure 4. Flat-plate predictions based on the *SA* model - sensitivity to spatial resolution (velocity and χ profiles correspond to *x/L*=0.6)

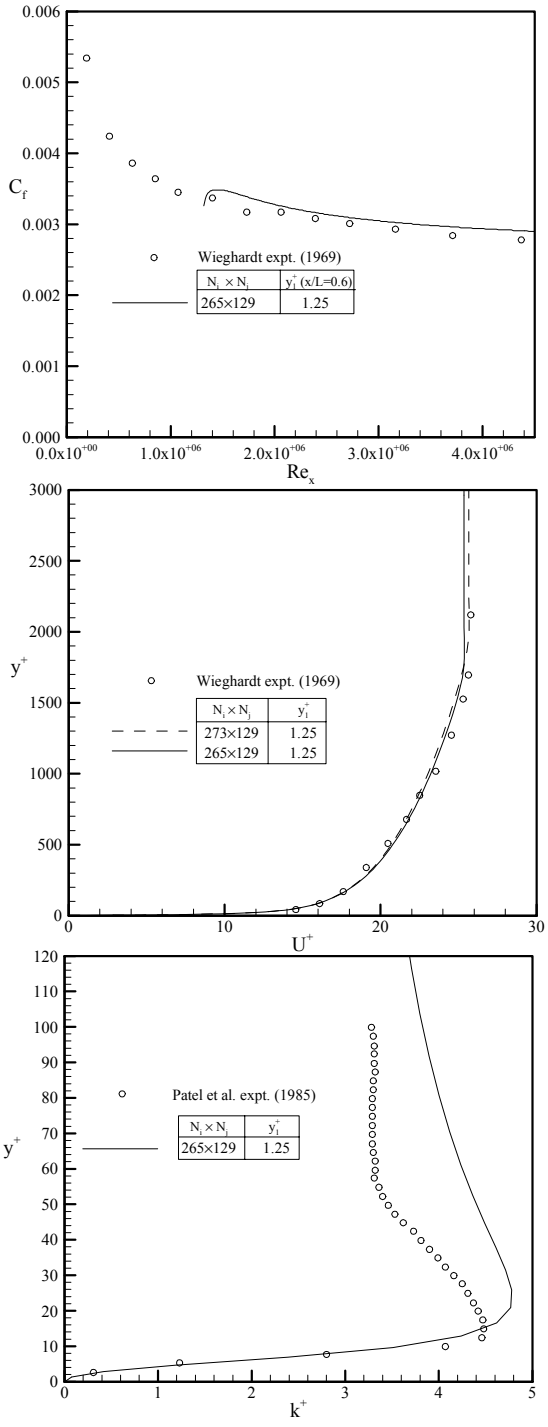

Figure 5. Flat-plate predictions based on Chien's k-ε model (velocity and k profiles correspond to x/L=0.6)

a slight error in polynomial representation of the inflow velocity profile very close to the plate surface. Interestingly, Chien's k-ε model is the only one that distinctly predicts the expected peak in k near the wall, albeit only qualitatively. Due to problems encountered with this model in the subsequent test flows, optimization of spatial resolution was not attempted for this model.

3.3.1 Sensitivity to Artificial Diffusion

In incompressible-flow simulations, the fourth-order artificial dissipation term, $D^{(4)}$, tends to be dominant since the pressure gradients are not steep enough to produce noticeable magnitudes for the second-order term. The effect of this artificial dissipation term on the prediction accuracy was evaluated through simulations with two different values of the scaling coefficient κ_4 : 0.005 and 0.01. Differences were apparent only on the coarser of the tested grids. This dependence of artificial dissipation on grid resolution is expected since node spacings dictate the distances over which the 4th order difference appearing in the artificial dissipation term is evaluated. Considering the close agreement between different grid resolutions in Figures 1 to 4 evaluated with κ_4=0.005, this κ_4 value is deemed sufficiently low to prevent numerical diffusion levels that would overshadow physical trends.

3.3.2 Sensitivity to Wall Boundary Conditions

Implementation of wall boundary conditions for each of the turbulence models was described earlier. A key parameter in the calculation of ω_{wall} for the *SST* model is β_{wall}. A value of 10 was proposed for this parameter by Menter [8], whereas Hellsten [20] noted that an increase of β_{wall} above 1.25 tends to amplify the dependence of the *SST* model predictions on grid resolution. Present simulations indicated the prediction accuracy to be very sensitive to changes in β_{wall} , with a value of 1.25 providing the best results.

3.3.3 Sensitivity to Freestream Turbulence Parameters

Simulations based on Rodi's k-ε model with $k = 1.3\times10^{-3}$ and a range of ε values from 1 to 100 in

the freestream resulted in essentially the same predictions of velocity and k distributions in the boundary layer. This observation in agreement with suggested values of freestream μ_e in the published literature [8, 24].

For both the k-ω and *SST* turbulence models, freestream values of ω, k and μ_e were systematically adjusted within the ranges of: ω = 100 to 5000; $k = 1.8\times10^{-6}$ to 1.8×10^{-3}; and $\mu_e/\mu = 2\times10^{-4}$ to 1×10^{-1}. The only noticeable sensitivity was noted to be with respect to the value of ω, with a value of 100 appearing as the best choice for both turbulence models. For the values of 100, 1000 and 5000 that were considered, the k-ω model displayed notable sensitivity to a change in ω from 100 to 1000, whereas variations in the predictions were only evident between ω values of 1000 and 5000 with the *SST* model.

Finally, sensitivity of the predictions with the *SA* model to freestream eddy viscosity was examined through variations of $\chi = \tilde{\nu}_e/\nu$ from 0.24 to 1.4, which corresponds to a μ_e/μ range from 1×10^{-5} to 1×10^{-2}. The changes in the predicted velocity and C_f distributions were negligibly small.

4 Simulations of Separating Flow in an Annular Diffuser

The axisymmetric, separating, adverse-pressure-gradient flow identified as Case C.S0 by Driver and Johnston [26] constituted the second test case of the present study. In this experiment, Driver and Johnston used an annular diffuser which was formed by aligning a cylinder longitudinally in a wind-tunnel test section with diverging walls. Boundary layer suction was applied at the test section walls such that separation occurred on the cylinder surface only. Prediction of the flow in this test case is particularly challenging since the separation bubble is not constrained in the axial direction.

4.1 Computational Domain

The size of the computational domain was minimized by prescribing a domain boundary at the larger radius that followed a stream-surface rather than extending the domain to the test-section walls. The shape of this stream-tube was defined on the basis of mass conservation. Figure 6 gives a cross-sectional view of the resulting axisymmetric computational domain. The computational domain was selected to be 1.26m long. The distance (R_S-R_0) between the surface of the inner cylinder and the outer slip-boundary ranged from a minimum of 0.037m at the inlet to a maximum of 0.071m in the region of separation.

4.2 Computational Grid

Grid dependence tests revealed that a minimum of 15 nodes were required in the boundary layer for each of the four turbulence models. The maximum allowable value for y_1^+ was found to be 5.0 for the *SA* and Rodi's k-ε models, while it had to be reduced to 1.3 for the other models. These results are consistent with the observations in the flat-plate simulations. For consistency, comparison of the predictions with different turbulence models against experimental data was based on a single grid that exceeds the minimum requirements of the most stringent turbulence model. For this purpose, a conservative grid was designed consisting of 89 and 61 nodes in the streamwise and radial directions, respectively, with y_1^+ =1.28 and about 40 nodes in the boundary layer at the inflow boundary. The variation of cross-stream clustering of the nodes with streamwise distance was chosen to ensure similar resolution of the boundary layer elsewhere.

4.3 Boundary Conditions and Iteration Parameters

Profiles of velocity and turbulence quantities were specified at the inflow boundary. The experimental data corresponding to the location of the inflow boundary of the computational domain (x =-0.457m) were found to agree well with the profiles of a simulated flat-plate boundary layer with the same Re_θ of 2760. Since the experimental profiles were relatively sparse, and not all of the turbulence quantities were part of the measured data set, the simulated flat-plate boundary layer data were used to specify the inflow boundary conditions. The

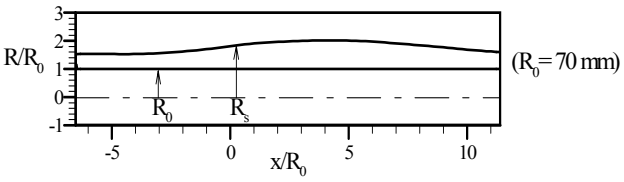

Figure 6. Computational domain used for Driver and Johnston's C.S0 test case

freestream velocity at the inflow boundary was set to 30 m/s as per the experiments. The values used for the turbulence quantities in the freestream portion of the inflow boundary were: $k = 1.3\times10^{-3}$, $\varepsilon = 7$ for the k-ε models of Rodi and Chien; $k = 1.8\times10^{-6}$, $\omega = 100$ for the k-ω and *SST* models; and χ=0.77 for the *SA* model.

At the outflow boundary the static pressure was set to a uniform value, and all other flow properties were extrapolated from the interior of the computational domain. It is well known that fixing of static pressure at an outflow boundary results in reflection of transient waves that develop during pseudo-time marching. To reduce the extent of this reflection, the following boundary condition was used for the outflow pressure, the compressible-flow version of which was originally proposed by Rudy and Strikwerda [27]:

$$\frac{\partial P}{\partial t} - \rho a_s \frac{\partial V_{local}}{\partial t} + \alpha_P \left(P - P_{BC} \right) = 0 \qquad (19)$$

where α_p is a constant set to 1/8 for the present test case, P_{BC} is the desired pressure value at the outflow boundary, and a_s, which is normally the speed of sound in a purely compressible flow solver, is evaluated as:

$$a_s = \sqrt{(V_{local})^2 + (c/a)^2} \qquad (20)$$

to reflect the preconditioned nature of the governing equations being solved by the present algorithm. Although the use of this less reflective outflow pressure boundary in the C.S0 test case substantially reduced the magnitude of the pressure oscillations during pseudo-time stepping, ultimate convergence to a solution was still not possible with two-grid-level multigrid cycles. After a sufficient number of multigrid cycles to develop the overall velocity and pressure fields, single-grid iterations were needed to complete the solution. These convergence difficulties encountered with this flow were absent in the simpler flat-plate test case, as well as the complex three-dimensional flows to be discussed in sections that follow. Separating flows in diffusing ducts, such as in the C.S0 test case, tend to be inherently unsteady. Even if a steady state is achieved in a well-controlled environment, which seems to be the case in Driver and Johnston's experiments, this state may easily be perturbed by small disturbances. The difficult-to-control transient behaviour observed numerically during pseudo-time stepping may be merely a reflection of this nature of the flow.

For optimum rates of convergence, the artificial compressibility parameter, c/a, was set to max[10.0m/s;$1.0V_{local}$], while the convective and diffusive time-step limits were determined on the basis of K_c=1.8, K_d=0.1. The artificial dissipation parameter, κ_4, was set to 0.005 as per the flat plate simulations. Initial and lower threshold settings of the turbulence parameters k, ε, ω and χ, were the same as those used in the flat plate simulations.

4.4 Simulation Results

As noted in Figure 7, all models reproduce the correct pressure distributions upstream and downstream of the separation bubble. The *SA* and *SST* models more accurately capture the flat portion of the C_p curve in the separated region. However, all model calculations result in over-prediction of static pressure in the region of separation. Based on the trends observed for C_f, separation is not predicted by Chien's k-ε model at all, and no flow reversal is captured by Rodi's k-ε model. The poor prediction of C_f by Chien's model was found to be related to periodic variations of

streamwise velocity along the length of the domain which prevailed along the first three grid lines next to the wall. Reduction of y_1^+ to values as low as 0.25 did not solve this problem. Similar C_f trends have been observed by Dudek et al. [28] and Shih [29], which suggests that this may be a fundamental deficiency of Chien's *k-ε* formulation. Due to this problem, and the requirement of limiting the turbulence production rate even for a flat-plate flow, Chien's *k-ε* model was excluded from the remainder of this study.

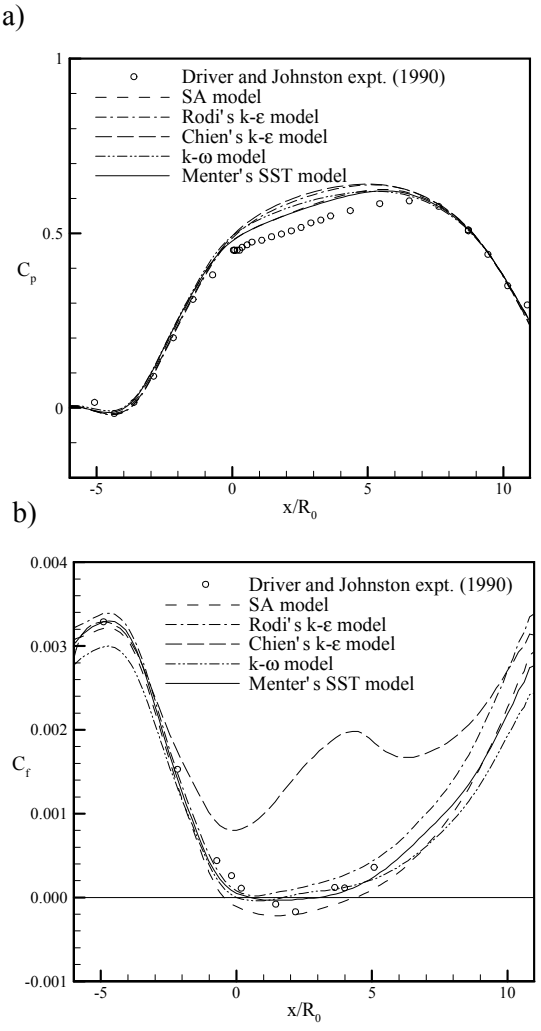

Figure 7. Comparison of C_p and C_f predictions with Driver and Johnston's experimental data

As presented in Figures 8 and 9, Menter's *SST* model is most successful in capturing the trends in the velocity field followed by the *SA* and *k-ω* models. Locations of separation and reattachment, summarized in Table 1, are also most accurately predicted by the *SST* model. Predictions of *k* profiles, shown in Figures 10 and 11, indicate a common trend for all models to underestimate the peak value. This trend is consistent with the results obtained for the flat plate boundary layer.

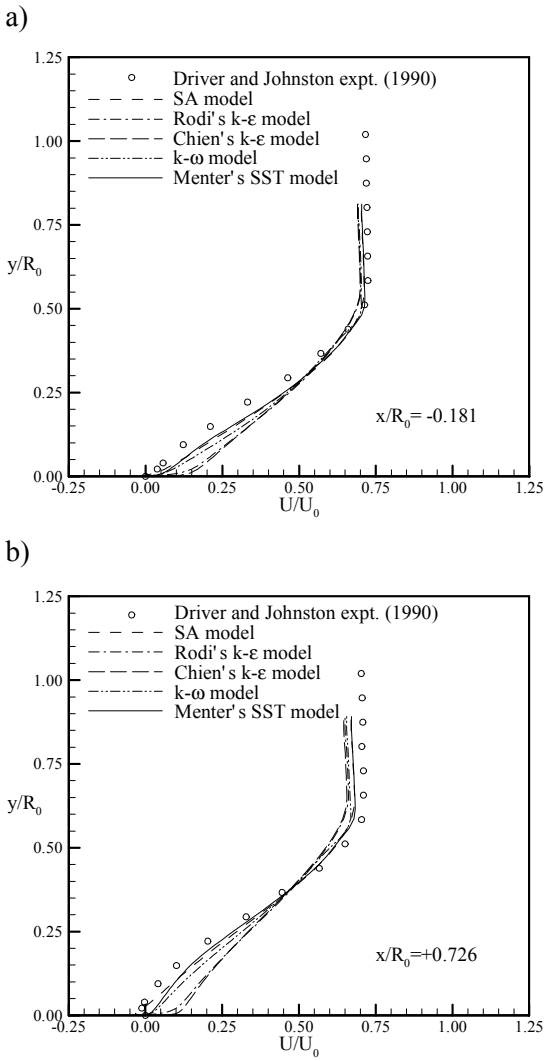

Figure 8 Comparison of predicted velocity profiles with Driver and Johnston's experimental data, a) x/R_0= -0.181, b) x/R_0= 0.726

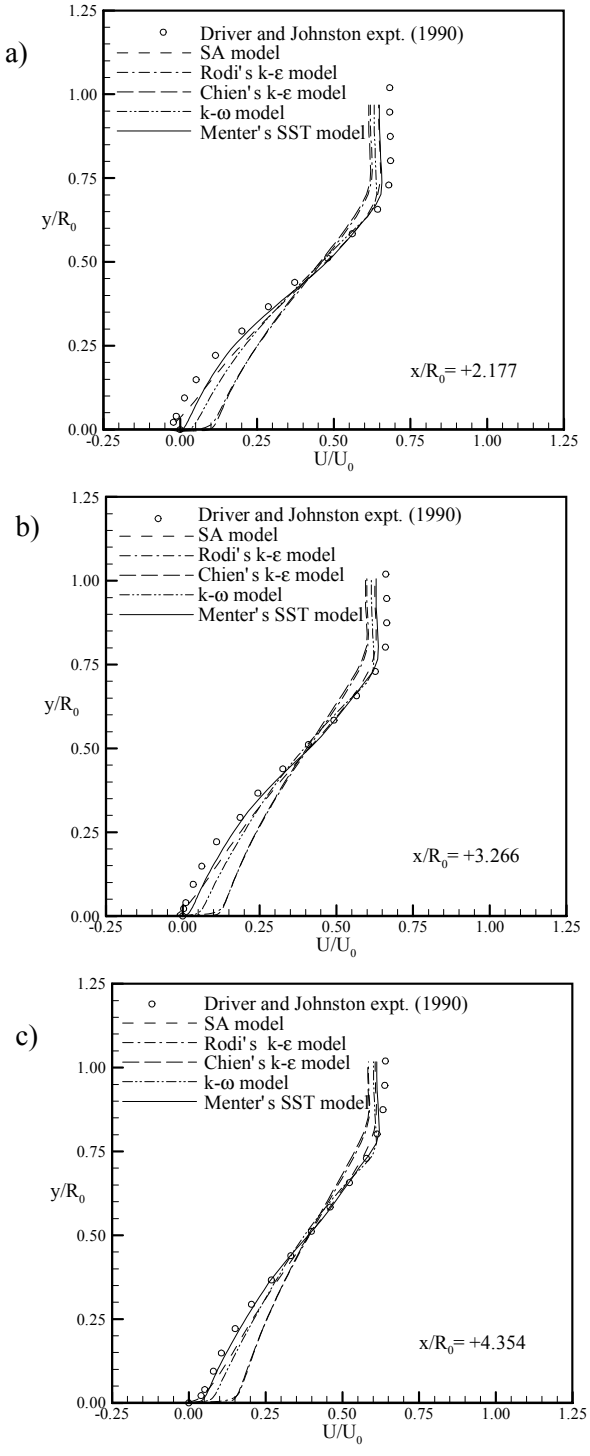

Figure 9. Comparison of predicted velocity profiles with Driver and Johnston's experimental data, a) x/R_0= 2.177, b) x/R_0= 3.266, c) x/R_0=4.354

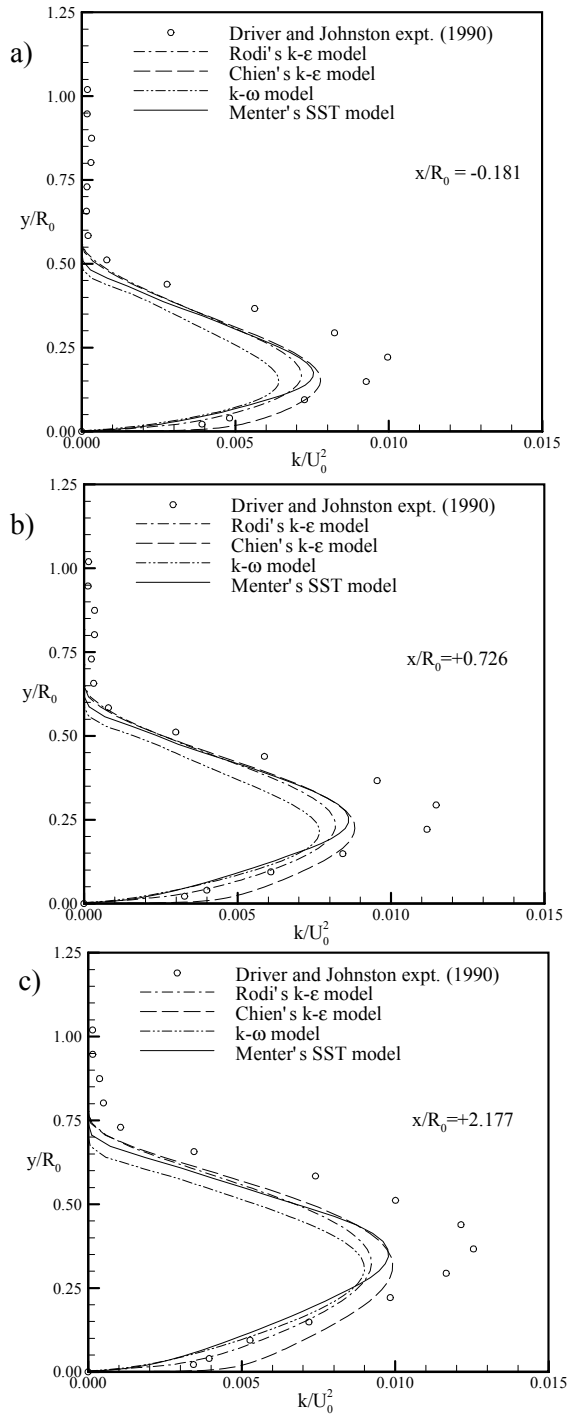

Figure 10. Comparison of predicted *k* profiles with Driver and Johnston's experimental data, a) x/R_0= -0.181, b) x/R_0= 0.726, c) x/R_0= 2.177

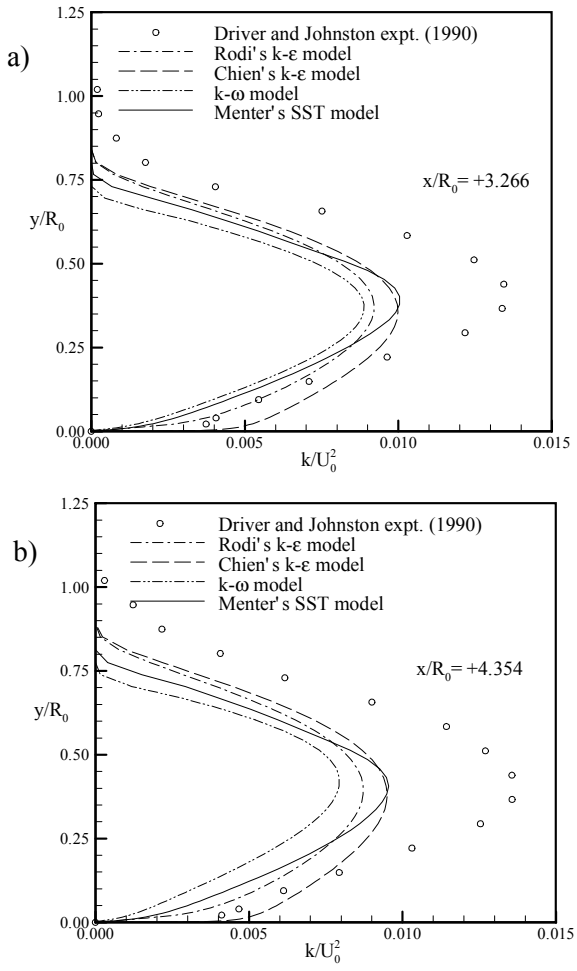

Figure 11. Comparison of predicted k profiles with Driver and Johnston's experimental data, a) x/R_0= 3.266, b) x/R_0= 4.354

	Exp.	*SA*	*k-ε*	*k-ω*	*SST*
x/R_0 - separation	0.6	-0.5	0.5	0.0	0.5
x/R_0 - reattachment	3.2	4.4	0.5	1.7	3.1

Table 1. Predicted separation and reattachment points compared with Driver and Johnston's experimental data (*k-ε* results correspond to Rodi's model)

5 Conclusions

The two-layer *k*-ε model of Rodi [6], the *k*-ω model of Wilcox [7], the two-equation shear-stress-transport model of Menter [8], the *k*-ε model of Chien [5] and the one-equation eddy-viscosity model of Spalart and Allmaras [9] have been evaluated for prediction accuracy and minimum spatial resolution requirements. The following main conclusions are drawn:

1. All turbulence models have been found to provide satisfactory development of the boundary layer over a flat plate in terms of velocity and surface shear stress distributions. At the same time, only Chien's *k*-ε model was able to reproduce the trends in the profile for turbulence kinetic energy, albeit only qualitatively.

2. All but Chien's *k*-ε model were fairly successful in capturing the surface pressure and skin friction distributions in an axisymmetric separating flow. A slight overprediction of the static pressure in the separated zone was common for the models. Menter's *SST* model was the most successful in capturing the trends in the velocity profiles followed by the *SA* and *k*-ω models; Rodi's *k*-ε model performed rather poorly in this respect. Those models that solve for the turbulence kinetic energy, *k,* failed to capture the peak *k* value in the boundary layer, which is consistent with the observations in the flat plate flow.

3. In terms of minimum grid resolution requirements for both the flat plate and the axisymmetric separating flows, Rodi's *k*-ε and the *SA* models showed the best performance, requiring a maximum of y_1^+=5 and at least 15 nodes within the boundary layer for acceptable prediction accuracy. The required minimum node count was about the same for the *k*-ω and *SST* models, whereas the upper limit for y_1^+ had to be set at about 1.3 for comparable accuracy.

An Evaluation of Several Low-Re Turbulence Models Part 2- Vortex-Generator-Jet Flows

M. I. Yaras
A.D. Grosvenor

Department of Mechanical and Aerospace Engineering
Carleton University, Ottawa, Ontario, CANADA K1S 5B6

Keywords: *turbulence modeling, separated flows, wall-jet vortex generators*

1 Introduction

This paper extends the evaluation of several one- and two-equation turbulence models contained in Part 1 of this study to include three-dimensional separated flows. In light of the performance of the turbulence models for the simpler flows of Part 1, only four of the five turbulence models in question are considered here. These are: the two-layer k-ε model of Rodi and his co-workers [6], the k-ω model of Wilcox [7], the two-equation shear-stress-transport model of Menter [8], and the one-equation eddy-viscosity model of Spalart and Allmaras [9]. The evaluation of these models is based on a vortex-generator jet flow [30]. This flow was chosen on the basis of availability of detailed, high-quality measurements, and the extent of challenging flow features such as three-dimensional boundary layers, three-dimensional flow separation / reattachment, and vortical flows it contains.

2 Simulations of a Vortex-Generator-Jet Flow

This section presents Vortex-Generator Jet (*VGJ*) predictions for Findlay's [30] vectored-jet-in-crossflow experiment. Findlay tested several combinations of θ (skew angle) and Φ (pitch angle). The configuration that is chosen as a test case (θ=-90°, Φ=30°) is not optimum with respect to boundary-layer control. Nonetheless, this configuration was chosen since the resultant turbulence levels in the wake of the jet were significantly higher than for the other configurations.

Streamwise vortices generated by the *VGJ*s are the key mechanisms in providing manipulation of the local flow field. In this respect, it is particularly important to accurately predict the cross-stream transport of momentum facilitated by these vortices which, in turn, requires precise prediction of their streamwise trajectory, concentration and diffusion rates. Therefore, the analysis of simulation results presented herein focuses on these aspects of the *VGJ* flow field.

2.1 Computational Domain, Boundary Conditions and Iteration Parameters

The simulated jet, depicted schematically in Figure 1, has an exit-plane cross-section of $1D \times 2D$. The jet Reynolds number, Re_D, based on the area-averaged jet velocity is 4910, and the jet-to-crossflow velocity ratio (*VR*) is 1.5. The crossflow freestream velocity is 3.84m/s, and at the upstream end of the computational domain (x = -5D), the boundary layer that had developed under zero pressure gradient reaches Re_θ= 445. The computational domain was chosen to extend 5D upstream of the jet exit, such that the inflow boundary remained unaffected by the jet flow field, and 11D in the downstream direction to include the flow region for which experimental data was available. The lateral extent of the computational domain was based on the spacing of the multiple jets in Findlay's experiments (=3D), and periodic

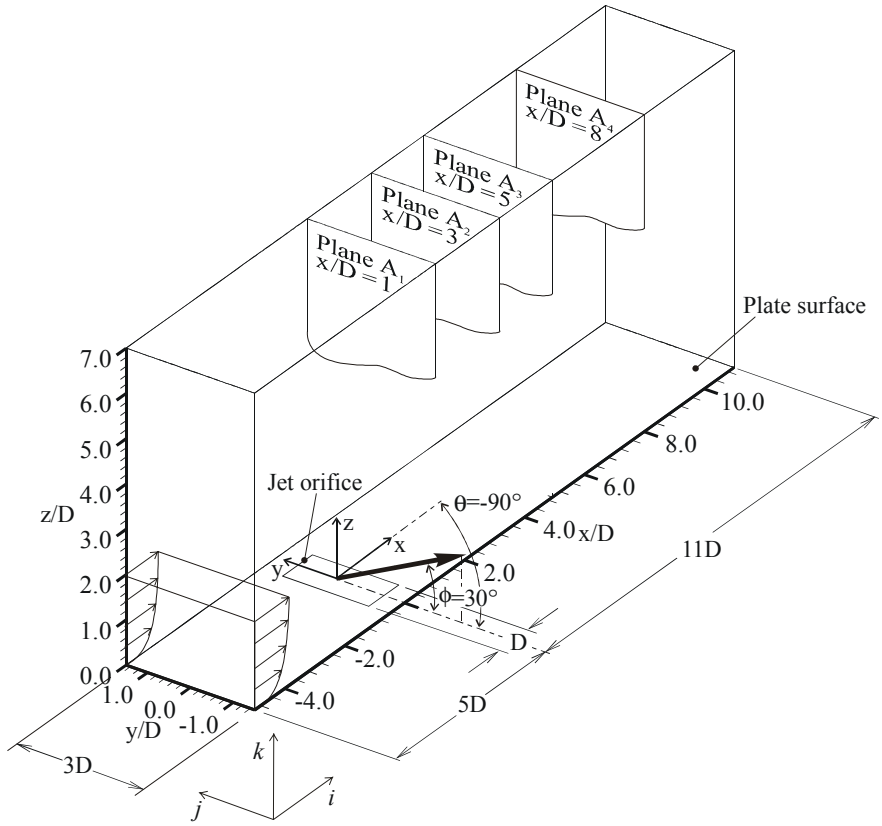

Figure 1. Computational domain for the *VGJ*

conditions were specified at the side boundaries.

At the top outflow boundary located at z/D=7, static pressure with a uniform distribution was specified and all other quantities were extrapolated from within the domain. It was also attempted to fix the static pressure at only a single node at this boundary and match the cross-stream pressure gradients in the plane of the boundary to those in the adjacent interior grid-plane. However, this adversely affected the rate of convergence to a solution. Specification of uniform pressure required the top boundary to be placed sufficiently above the jet exit to prevent it from interfering with the natural development of vortex roll-up and subsequent diffusion. Several locations were considered for this boundary to establish sensitivity of the predicted flow field to the size of the computational domain. Upon setting the pressure at the top outflow boundary, no pressure specification was required at the aft outflow boundary located at x/D=11.

The freestream velocity at the inflow boundary for the crossflow (x=-5D) was set to 3.84m/s as per Findlay's experimental conditions. The flow direction was aligned with the x-axis and the turbulence parameters were set to: $k = 1.3\times10^{-3}$, $\varepsilon = 7$ for Rodi's k-ε model; $k = 1.8\times10^{-6}$, $\omega = 100$ for the k-ω and *SST* models; and $\chi = 0.77$ for the *SA* model. The profiles of velocity and k in the crossflow boundary layer (Re_θ=445, $\delta \approx 2D$) were obtained from polynomial curve fits to the experimental data, and the remaining turbulence properties (ε, ω and χ) were obtained from separately-performed flat-plate simulations.

The remaining boundary condition that requires some consideration is the inflow boundary for the jet. It is well known that the distributions of velocity and turbulence quantities at this boundary are generally far from being uniform. A number of simulation studies have included in the computational domain the pipe leading to the jet-exit plane [31,32], and even the plenum feeding the pipe. There have also been studies

that completely ignored the nonuniformity of the flow at the jet-exit plane [33,34].

In the context of industrial calculations involving multiple *VGJ*s, inclusion of jet pipes, and possibly plenums feeding these pipes, into the computational domain is undesirable since its impact on computing time would be significant. In the present simulations, the jet inflow boundary conditions were specified right at the exit plane of the jet. The ultimate objective was to simply impose uniform flow conditions at this inflow boundary, as has been done by several other researchers. To justify this approach, however, simulations were also performed with nonuniform flow at the jet-exit plane for comparison. For these nonuniform conditions, polynomial chi-square surface fits were performed to the velocity magnitude, flow direction, and turbulence kinetic energy data of Findlay [30]. These polynomial approximations had to be implemented in patches to ensure reasonable agreement with the experimental data. Figure 2 shows the extent of flow nonuniformity at the jet exit plane, and the polynomial surface fits used in the simulations. Surface fits for flow direction were of similar quality, and are not shown here since the variation in flow direction was small (less than 10 degrees). For simulations with uniform flow conditions at the jet exit plane, average values of velocity magnitude, direction and turbulence kinetic energy were used. Variation of ε in the jet-exit plane was determined using:

$$\varepsilon = \frac{k^{3/2}}{0.2 D_h} \qquad (1)$$

from which distributions of ω and $\tilde{\nu}$ could be readily calculated.

For optimum rates of convergence, the artificial compressibility parameter, c/a, was set to max[3.0m/s;2.0V_{local}], while the convective and diffusive time-step limits were determined on the basis of K_c=1.8, K_d=0.1. The artificial dissipation parameter, κ_4 , was set again to 0.005. Initial and lower threshold settings of the turbulence parameters k, ε, ω and χ, were also the same as those used in the previous test cases. For Rodi's k-ε model, the turbulence production-to-destruction ratio of ($\mathcal{P}_k/\mathcal{D}_k$) had to be limited to 20 to prevent divergence of the solution. The unbounded growth of this ratio tended to take place in the shear layer between the jet and crossflow, upstream of the roll-up process.

2.2 Computational Grid

In identifying the optimum grid configuration, a series of grids were chosen that systematically provided local refinement in strategically selected portions of the computational domain where spatial gradients in the flow field were relatively high. Specifically, emphasis was placed on establishing sufficient resolution in the vorticity field downstream of the jet orifice, in the core region of the jet, and along the perimeter of the jet. In proximity of the wall surface (z/D=0.0), resolution in the z direction was fixed based on the requirement of y_1^+=1.25 and a minimum of 15 nodes in the boundary layer, established in the previous test cases to be adequate for all the turbulence models in question. In addition to the node count, locations of the top and aft outflow boundaries were also varied to establish sensitivity of the predicted flow to the size of the computational domain. The ultimate objective of such a node-count and domain-size- optimisation exercise is to identify the best combination of these parameters that would allow accurate prediction of the *VGJ* flow in the shortest time. It must be mentioned that the current optimisation is specific to the *VGJ* configuration being considered with respect to θ, Φ, *VR* and lateral jet spacing. Nonetheless, it should be possible to extrapolate from the present results to establish first-order estimates of minimum grid / domain size requirements of alternative *VGJ* configurations.

The tested grid and computational-domain-size combinations are summarized in Table 1, and are displayed in Figure 3. Between these grids, the maximum variations in the local velocity components were within about 6% of $\overline{V}_J$, whereas k, and Ω_x varied within about 5% of the maximum values encountered in the computational domain.

Since the amount of artificial dissipation affecting the solution is related to the spatial resolution, it is essential that any grid optimisation study be

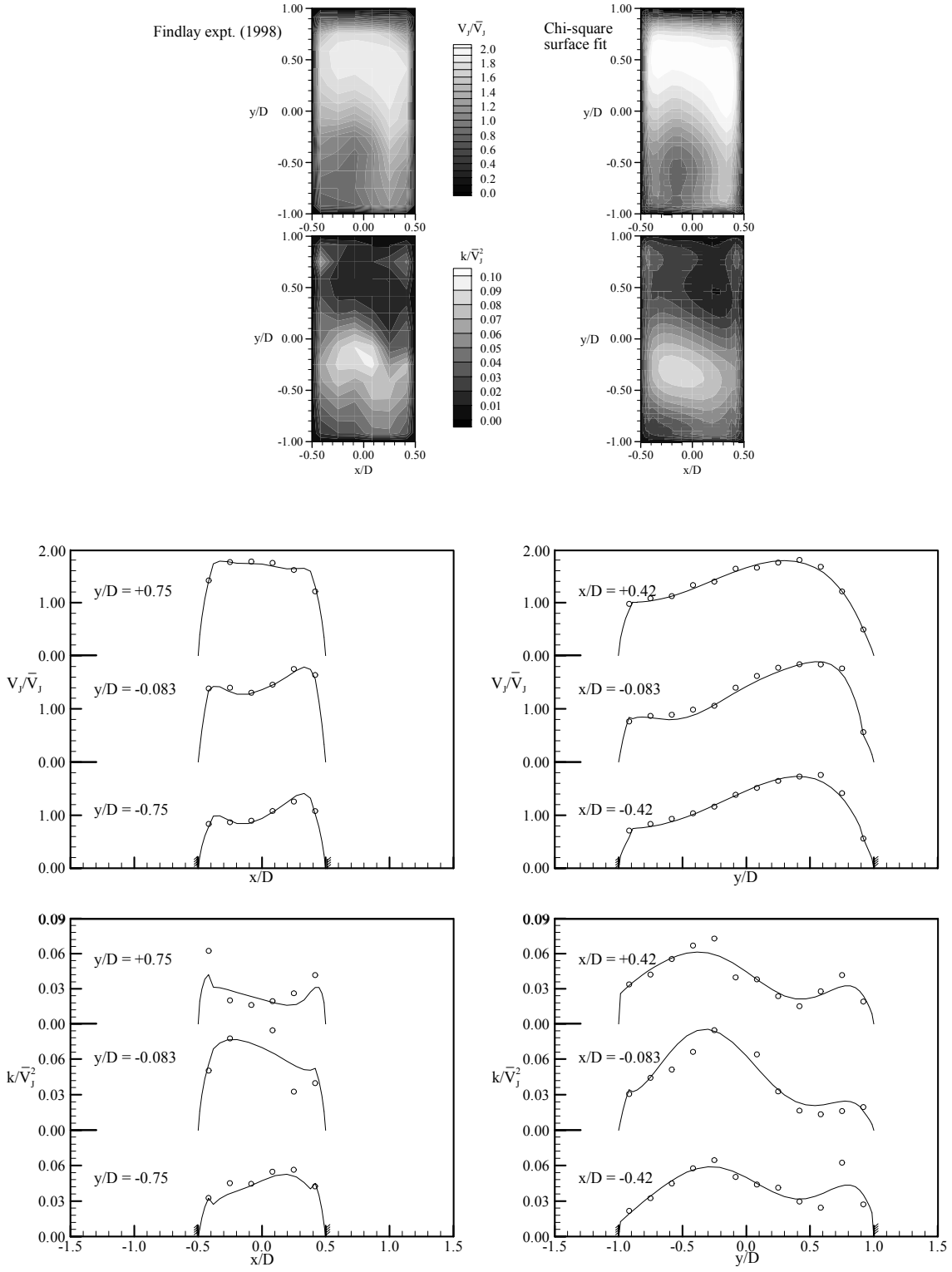

Figure 2. Distributions of V_J and k at the jet exit plane,
◦ Findlay expt. (1998), ——— Surface fit

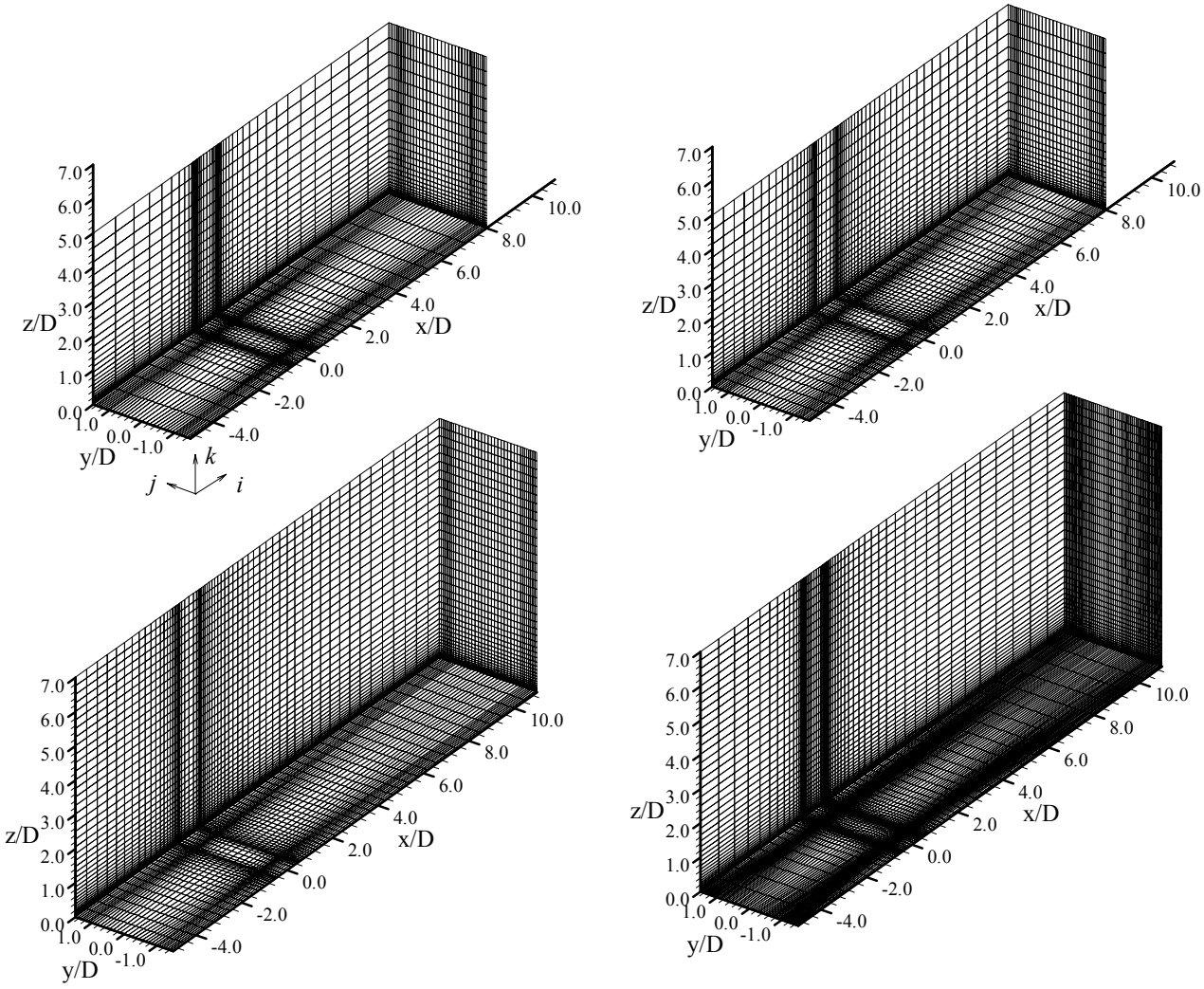

Figure 3. Node distributions for the *VGJ* simulations

performed in this context. Simulations were thus performed with values of 0.005 and 0.01 for κ_4, the scaling factor for the 4th order artificial dissipation term. On the coarsest grid considered, the sensitivity to κ_4 was about 2.5% of $\overline{V}_J$ for the local velocity components, 6% for k and 3.5% for Ω_x with respect to their maximum values within the computational domain. This sensitivity was notably less on Grid D.

Based on these sensitivity analyses, Grid A can be judged to be adequate for computations that are time-critical in an industrial setting. However, to maximize the accuracy in the comparisons of turbulence models and alternative considerations of jet-exit boundary conditions presented herein, the simulations were based on the more conservative spatial resolution and domain size of Grid D.

Grid	N_i	N_j	N_k	Number of nodes in:			Largest grid cell	Top outflow (z/D)	Aft outflow (x/D)
				inflow boundary layer	jet core*	jet shear layer*			
A	47	37	29	20	11	7	1D	5	8
B	59	37	29	20	9	5	1/2D	5	8
C	65	37	43	20	9	5	1/2D	7	11
D	69	61	43	20	15	9	3/4D	7	11

Table1. Grid details for the *VGJ* simulations
* these node counts relate to the flow region just above the jet orifice

2.3 Description of Flow Physics

Prior to discussions of prediction sensitivity to the choice of grid, boundary conditions and turbulence-models, a typical set of results of these simulations is presented here to examine the physics of the flow. The main features of the *VGJ* flow field predicted with Menter's *SST* model are depicted in Figure 4. The velocity, streamwise vorticity (Ω_x), and turbulent kinetic energy (k) fields, as well as the surface C_f distribution in the near-field of the jet, accompanied by streamlines at the first set of nodes off the wall are displayed.

A significant spanwise velocity component, with peak magnitudes comparable to the initial jet velocity, is observed to persist as far as 8D downstream of the jet orifice, which is the result of the shallow pitch angle and spanwise orientation of the jet combined with the relatively large jet-to-crossflow velocity ratio. A single dominant streamwise vortex is noted to develop but is observed to be relatively weak at the start, and loses its strength rapidly with downstream distance. Presence of this vortex, combined with the small initial pitch angle of the jet, are most likely responsible for the collective reorientation of the cross-stream velocity component from the initial 30° towards 0° within about 1.5D downstream distance. Before studying the crossflow velocity and streamwise vorticity distributions further, examination of the vector field topology (Figure 4d) should help to shed light on the overall flow development.

The stagnation point in front of the jet is indicated by the saddle of separation *Ss1*. The location of this point is biassed toward the negative y direction relative to the centre of the jet orifice due to the large jet skew angle. The same trend was observed by Barberopoulos and Garry [35] for a jet at 60° skew angle. Negative bifurcation lines (*NBL1,2*), or three-dimensional lines of separation, extend out from *Ss1* in the negative and positive y directions providing an indication of the extent of the separated (recirculating) region in front of the jet. Due to the close proximity of the adjacent jets in the present test case, both of the *NBL*'s lead into separation saddles (*Ss2*) at the jet orifice. Thus, instead of wrapping around the jet and augmenting focus nodes *F1* and *F2*, as is the case for a single jet [35], the *NBL*s are blocked. This would be expected to produce a weaker streamwise vortex behind the orifice and also explains why horseshoe vortices cannot be discerned from the velocity or vorticity plots downstream of the jet orifice. A node of attachment (*Na1*) follows *Ss1* and feeds two focus nodes of separation (*F1* and *F2*) at the corner x/D=0.5, y/D=-1.0 which constitute the starting point of the dominant streamwise vortex. The close proximity of the two focus nodes to each other is due to the high skew angle of the present jet. This pattern has also been observed by Barberopoulos and Garry for their jet at 60°skew.

Having identified the origin of the dominant streamwise vortex from the surface vector topology, the remaining details of the vortex development can be discerned from parts (a), (b) and (c) of Figure 4. At plane A_1 , the negative vorticity field associated with this vortex is seen to be partially annihilated on the upwash side by positive vorticity convected away from the boundary layer. Further downstream, in

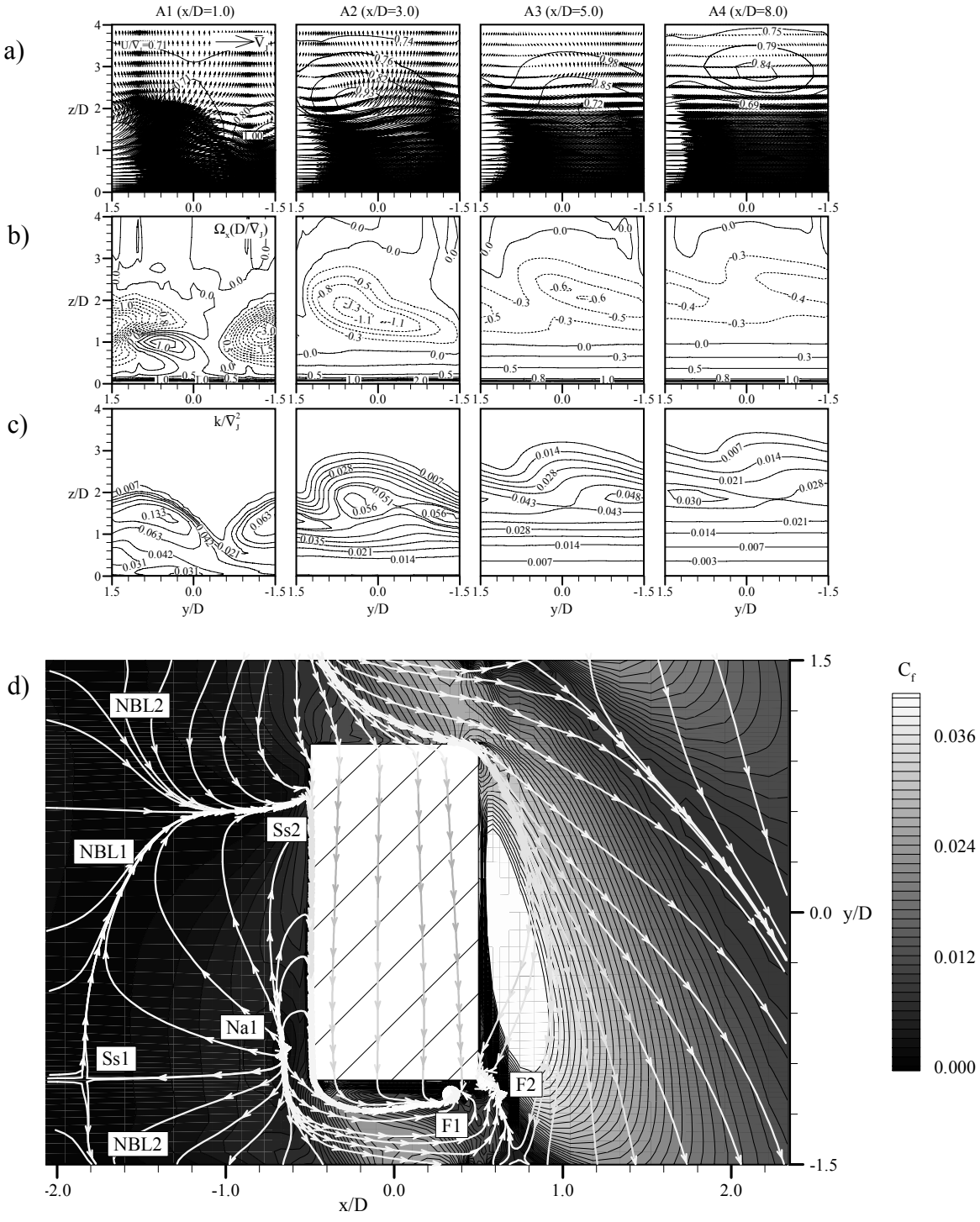

Figure 4. Features of the *VGJ* flowfield, based on Menter's *SST* model
a) Cross-flow velocity vectors (V,W) and U contours,
b) Ω_x contours (negative values indicated by dashed lines),
c) k contours, d) C_f and streamlines at first node off the wall

planes A_2, A_3 and A_4, this partially annihilated region is noted to contribute to the spanwise smearing of the negative vorticity field as it rotates and stretches. This smearing effect, in turn, is reflected in the cross-stream distribution of k. These observations are supported by the results of Khan [36] who noted lower vorticity magnitudes and higher deformation of the vorticity field at a skew angle (θ) of 90° compared to θ=60°, the latter of which he deemed to be the optimum value for boundary layer control at Φ=30° and VR=1.0.

2.4 Simulation Results

Prediction results for the four turbulence models in question are shown in Figures 5 to 11. The value of maximum streamwise vorticity, displayed in Figure 5a, is predicted reasonably well with Rodi's k-ε and the k-ω models, while the *SA* and *SST* models yield very good results. As far as the location of this peak vorticity, shown in Figure 6a, all models predict a trajectory that is slightly further away from the wall surface than the measured one, with the discrepancy increasing further downstream, and the lateral convection of the vortex is slightly overestimated. At each streamwise location (Figures 7 to 10), the value of U is underpredicted in close vicinity of the wall which may be in part due to underestimation of the cross-stream transfer of momentum by the streamwise vortex developing with downstream distance. Generally, all models appear to produce similar distributions, although Rodi's k-ε model is outperformed by the remaining models in capturing the trends in the turbulence kinetic energy, the y-velocity component, V, and to a lesser extent, the z-velocity component, W.

In summary, the difference between the prediction accuracies of the four turbulence models is not very large. There is consistent evidence, however, that the predictions with Rodi's k-ε model are slightly inferior to those with the remaining models in certain respects. Specifically, all models are capable of capturing the overall rate of diffusion of the streamwise vortex with downstream distance and the trajectory of this vortex, but predictions of the details of the velocity field,

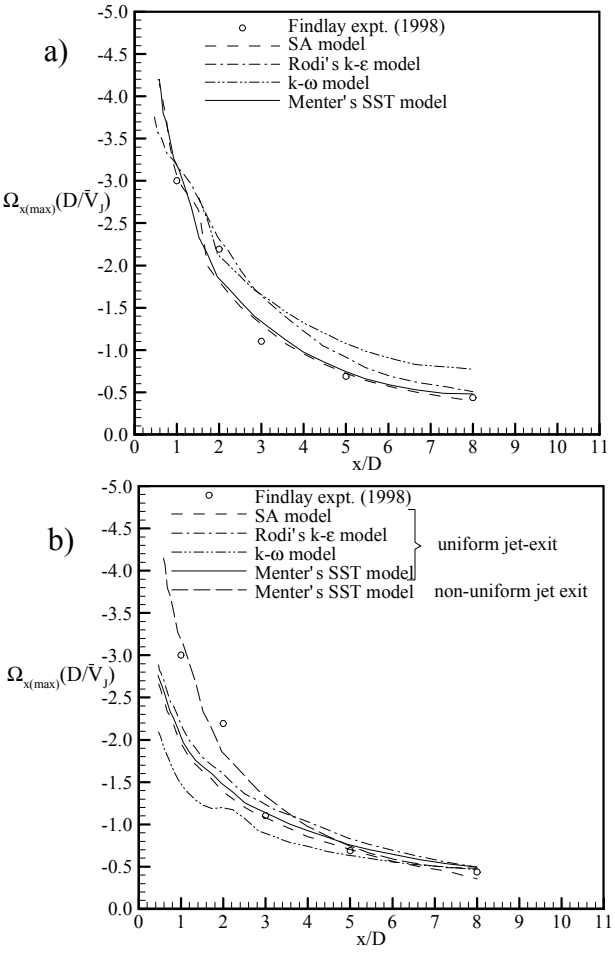

Figure 5 Predicted maximum streamwise vorticity in the jet-induced vorticity field:
a) sensitivity to turbulence models
b) sensitivity to jet boundary conditions

hence the extent of cross-stream mass and momentum transfer are not as accurate, with Rodi's k-ε model trailing the other ones in this respect.

Although it is best to base such simulations on an accurate description of the flow nonuniformity at the jet exit plane, such a treatment is not practical since the type of nonuniformity would depend significantly on the jet configuration, the details of the jet pipe and plenum design, as well as the crossflow conditions.

For the present approach of specifying inflow boundary conditions at the jet exit plane to be

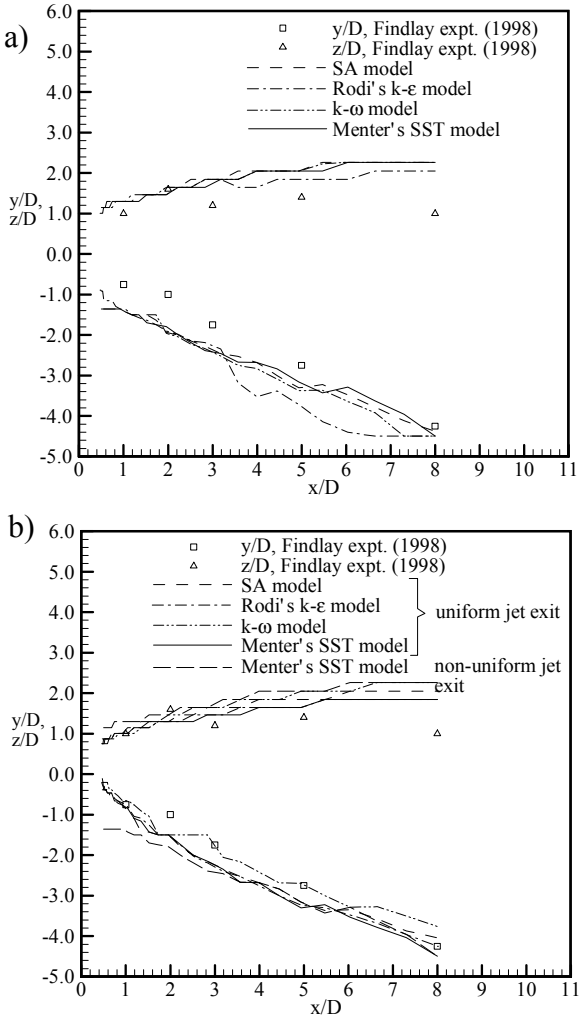

Figure 6. Predicted location of max. streamwise vorticity in the jet-induced vorticity field: a) sensitivity to turbulence models b) sensitivity to jet boundary conditions

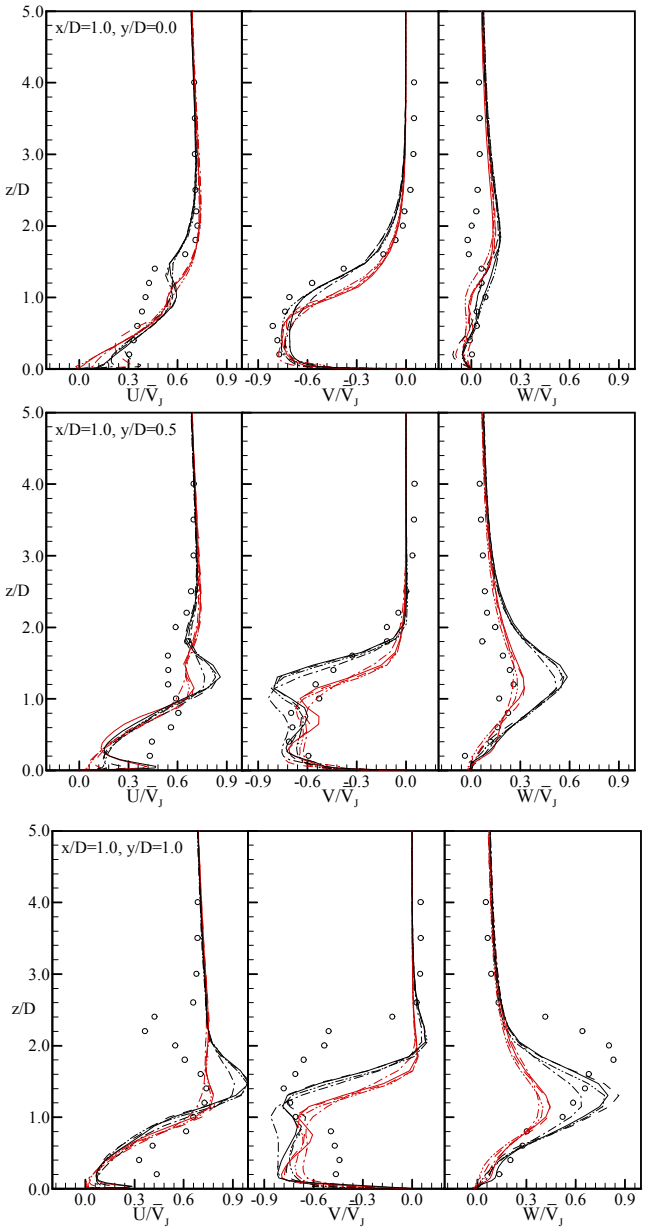

Figure 7. Comparison of predicted velocity profiles in plane A_1 with experimental data: sensitivity to turbulence models and jet boundary condition
◦ Findlay's expt. (1998), – – – *SA* model, – · – · – Rodi's *k-ε* model, – · · – · · – *k-ω* model, —— Menter's *SST* model
(red curves: uniform jet-exit flow; black curves: nonuniform jet-exit flow)

practical, a more generic distribution must suffice. Sensitivity of the *VGJ* flow field to this jet boundary condition was therefore tested by comparing predictions with uniform distributions of velocity and turbulence quantities to the original, nonuniform results. The velocity magnitude was adjusted to match the mass flow of the nonuniform case, hence maintaining the same jet-to-crossflow velocity ratio. As for the nonuniform case, a thin boundary layer (δ=0.16D) was specified along the perimeter of the jet orifice, so as to avoid sharp velocity gradients that

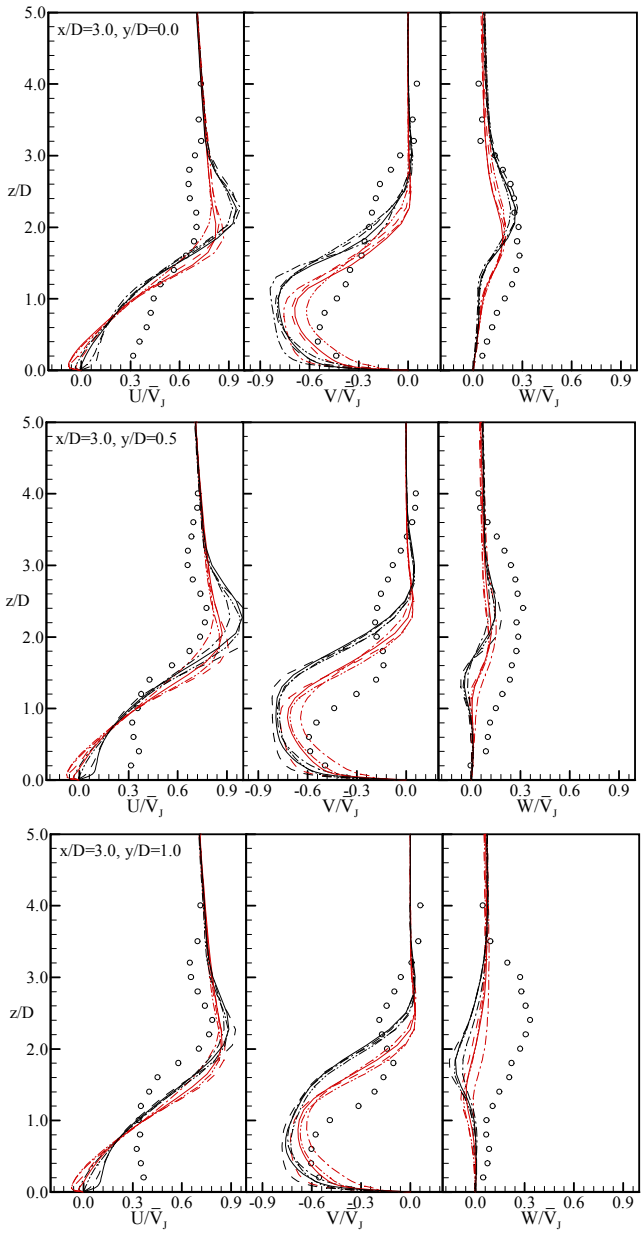

Figure 8. Comparison of predicted velocity profiles in plane A_2 with experimental data: sensitivity to turbulence models and jet boundary condition (see Fig. 7 for symbols and lines)

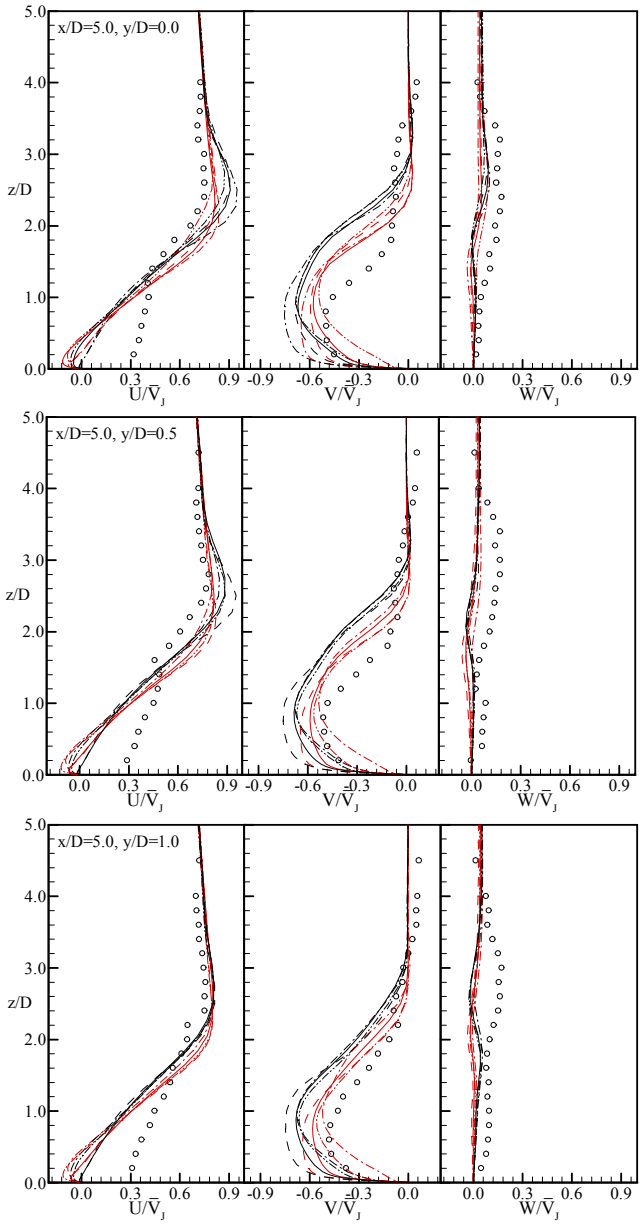

Figure 9. Comparison of predicted velocity profiles in plane A_3 with experimental data: sensitivity to turbulence models and jet boundary condition (see Fig. 7 for symbols and lines)

may have triggered solution instability due to excessive levels of shear. An average k value was calculated from the nonuniform distribution and was specified along with a uniform ε value calculated from this k value using Eqn. 1.

The results with uniform jet-exit conditions are shown in Figures 5b, 6b, and with red color in Figures 7 to 11. Distinct deviations are noted in these figures from the results with nonuniform treatment of the jet-exit

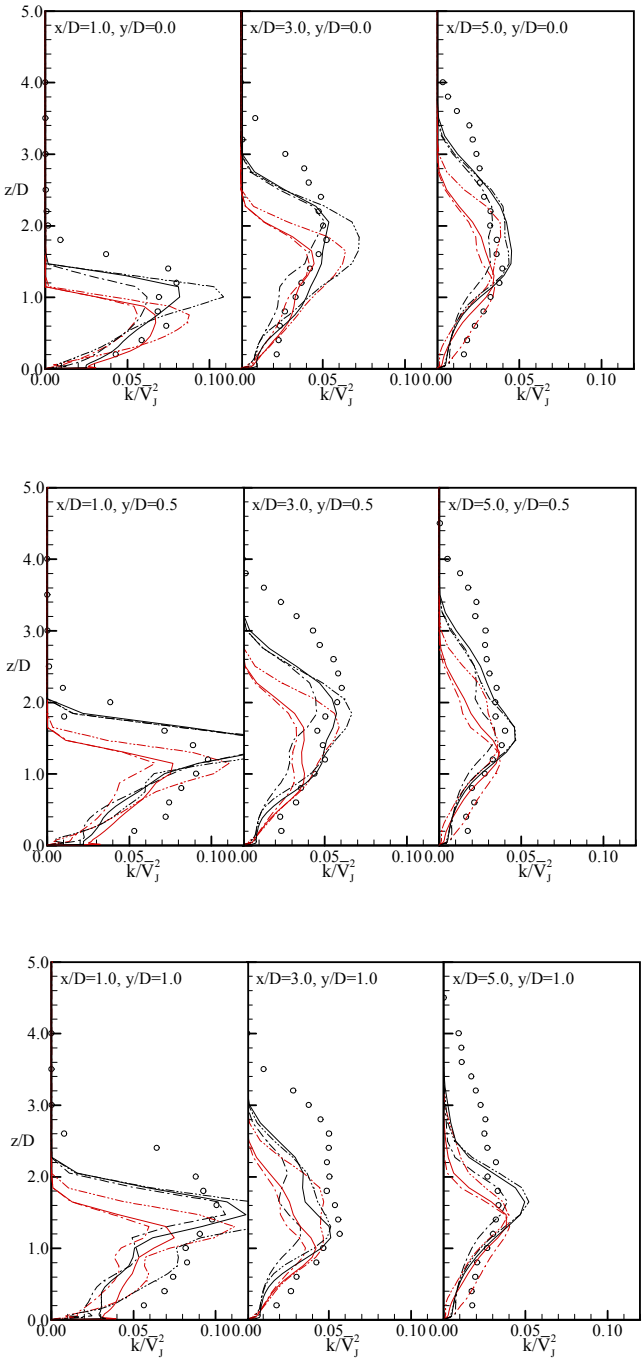

Figure 10 Comparison of predicted *k* profiles (planes A_1, A_2, A_3) with experimental data: sensitivity to turbulence models and jet boundary condition (see Fig. 7 for description of symbols and lines)

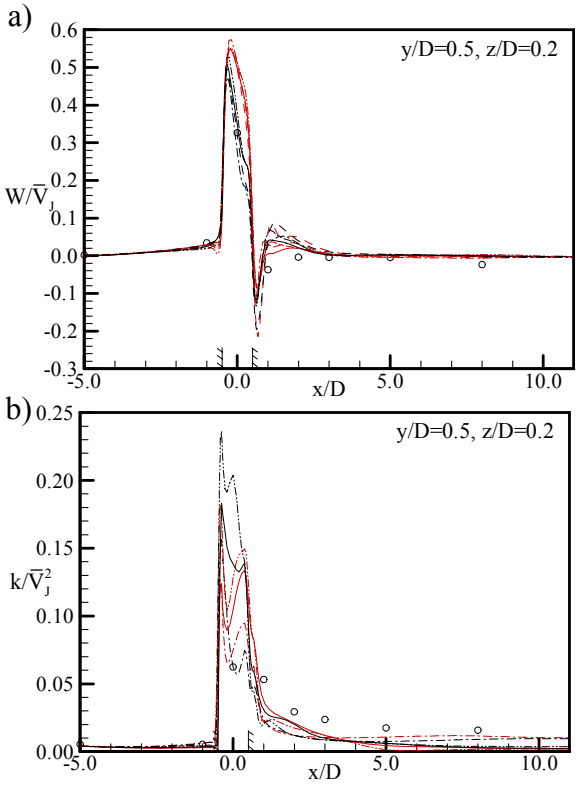

Figure 11. Comparison of predicted velocity and k profiles with experimental data: a) *W* and b) *k* across shear layer - sensitivity to turbulence models and jet boundary condition (see Fig. 7 for description of symbols and lines)

plane. However, these variations are noted to be generally within the margin of error of the simulations with respect to experimental results. It thus appears that uniform boundary conditions may be imposed at the jet-exit plane without notable changes in prediction accuracy when one of the present turbulence models is used. However, it should be noted that this statement is based on tests with a relatively high *VR*, and there is some evidence that it may not be applicable to lower *VR* values. For example, Findlay [30] observed higher flow nonuniformity at the jet exit plane with decrease in *VR*, and Khan [36] noted that the turning of the jet flow was already initiated before leaving the jet hole for a *VGJ* with *VR*=1.0.

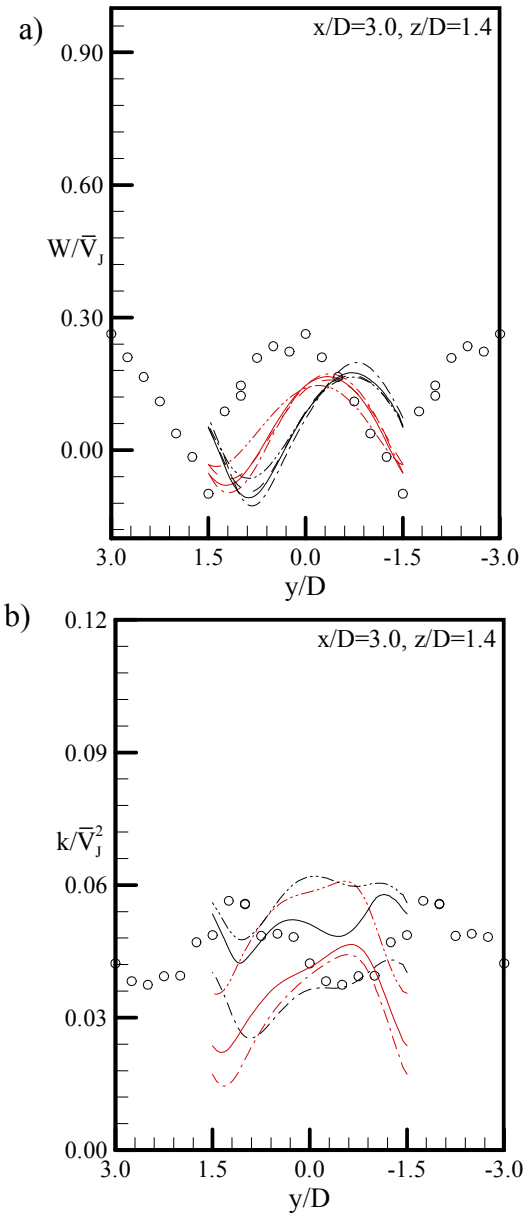

Figure 12. Comparison of predicted velocity and k profiles with experimental data: a) *W* and b) *k* across streamwise vorticity field - sensitivity to turbulence models and jet boundary condition (see Fig. 7 for description of symbols and lines)

3 Conclusions

The two-layer *k*-ε model of Rodi [6], the *k*-*ω* model of Wilcox [7], the two-equation shear-stress-transport model of Menter [8], and the one-equation eddy-viscosity model of Spalart and Allmaras [9] were further evaluated for a complex three dimensional flow, based on near-wall spatial resolutions that were established in Part-1 of this study. The following main conclusions are drawn:

1. Simulations were performed for a periodic vortex-generator-jet (*VGJ*) flow of 30 deg. pitch, 90 deg. skew, a jet-to-crossflow velocity ratio of 1.5, and an approach boundary layer thickness of about twice the streamwise dimension of the jet orifice (*D*). For this configuration, node counts of 47, 37 and 29 in the streamwise, spanwise and vertical directions were found to be sufficient to yield essentially grid-independent results with the computational domain being 13*D* long , 5*D* high and 3*D* wide. Accounting for the flow nonuniformity at the jet orifice inflow boundary was found to have a noticeable effect on the prediction accuracy. However, the extent of this effect was observed to be comparable to the typical difference between measured data and predictions based on any one of the turbulence models considered.

2. The difference between the prediction accuracies of the four turbulence models (Rodi's *k*-ε, Menter's *SST*, *k*-*ω*, and *SA*) in the *VGJ* flow was not very significant. However, the predictions with Rodi's *k*-*ε* model were noted to be consistently less accurate than with the remaining models in certain respects. Specifically, all four models were able to reproduce the rate of diffusion of the streamwise vortex with downstream distance and the trajectory of this vortex reasonably well, but predictions of the overall velocity field, hence the extent of cross-stream mass and momentum transfer were not as accurate, with Rodi's *k*-*ε* model trailing the other models in this respect.

3. Considering all of the test cases examined in Parts 1 and 2 of this study, the one-equation model of Spalart and Allmaras [9] was found to provide the best combination of: minimum resolution requirements of wall boundary layers, consistent prediction accuracy, robustness and computational efficiency.

A byproduct of the present study is the evaluation of a particular Navier-Stokes (*NS*) algorithm for three-dimensional separated flows. It has been demonstrated that iterative solution of the *NS* equations through alternating implicit/explicit pseudo-time marching based on two-stage *Runge-Kutta* integration, combined with local sizing of pseudo-time steps and a multigrid procedure as acceleration schemes, is an efficient and robust algorithm for such flows. Additionally, explicit control over artificial dissipation terms facilitated by the algorithm has been shown to be very effective in being able to suppress the development of spurious spatial oscillations, without introducing excessive numerical diffusion into the solution that would undermine the predictive capability of the turbulence models. Finally, the capability of a certain type of preconditioning of the mass and momentum equations to allow monotonic and efficient convergence in the incompressible regime has been demonstrated, and appropriate settings for the relevant preconditioning parameters have been provided.

References

[1] Iacovides H, Launder BE. The Numerical Simulation of Flow and Heat Transfer in Tubes in Orthogonal-Mode Rotation. In *Proc. 6th Symp. On Turbulent Shear Flows*. 1987.

[2] Patel VC, Rodi W, Scheuerer G. Turbulence Models for Near-Wall and Low-Reynolds-Number Flows: A Review. *AIAA J.* 1985; **23**: 1308-1319.

[3] Shih TH, Mansour NN. Modelling of Near-Wall Turbulence. In *Engineering Turbulence Modelling and Experiments*, Rodi W and Ganic EN (eds), Elsevier; 1990; pp 13-22.

[4] Rodi W. Experience with Two-Layer Models Combining the *k-ε* Model with a One-Equation Model Near the Wall. *AIAA Paper 91-0216*; 1991.

[5] Chien K-Y. Prediction of Channel and Boundary Layer Flows with a Low-Reynolds- Number Turbulence Model. *AIAA J.* 1982; **20**: 33-38.

[6] Rodi W. Recent Developments in Turbulence Modeling. In *Proc. 3rd Int. Symp. on Refined Flow Modeling and Turbulence Measurements*, Iwasa Y., Tamai N. and Wada A. (eds.), Tokyo, Japan; 1988.

[7] Wilcox DC. *Turbulence Modeling for CFD*, 2nd ed. DCW Industries; 1988.

[8] Menter, FR. Eddy Viscosity Transport Models and their Relation to the *k-ε* Model. *NASA Technical Memorandum TM-108854*; 1994.

[9] Spalart PR, Allmaras, SR. A One Equation Turbulence Model for Aerodynamic Flows. *AIAA Paper 92-0439*; 1992.

[10] Crumpton PI, Shaw GJ. A Vertex-Centered Finite Volume Method with Shock Detection. *Int. Journal for Numerical Methods in Fluids*; 1994; **18**: 605-625.

[11] Jameson A., Schmidt W, Turkel E. Numerical Solutions of the Euler Equations by Finite Volume Methods using Runge-Kutta Time-Stepping Schemes. *AIAA Paper 81-1259*; 1981.

[12] Swanson RC, Turkel E. Artificial Dissipation and Central Difference Schemes for the Euler and Navier Stokes Equations. *AIAA Paper 87-1107*; 1987.

[13] Turkel E, Vatsa VN. Effect of Artificial Viscosity on Three-Dimensional Flow Solutions. *AIAA Journal*; 1994; **32**: 39-45.

[14] Lin FB, Sotiropoulos F. Assessment of Artificial Dissipation Models for Three Dimensional Incompressible Flow Solutions. *Journal of Fluids Engineering*; 1997; **119**: 331-340.

[15] Turkel E. Preconditioned Methods for Solving the Incompressible and Low Speed Compressible Equations. *J. of Comp. Phys.* 1987; **72**: 277-298.

[16] Stone HL. Iterative Solution of Implicit Approximation of Multidimensional Partial Differential Equations. *SIAM J. of Numerical Analysis*; 1968; , **5**:530-558.

[17] Schneider GE, Zedan M. A modified Strongly Implicit Procedure for the Numerical Solution of Field Problems. *J. of Numerical Heat Transfer*; 1981; **4**:1-19.

[18] Brandt A. Multi-Level Adaptive Solutions to Boundary Value Problems. *Mathematics of Computation;* 1977; **31**:333-390.

[19] Yaras MI. Grosvenor AD. Numerical Simulations of Diffusing S-Duct and Vortex-Generator-Jet Flows. *National Research Council of Canada Contract Report no. 31184-8-8847/001/ST;*2000.

[20] Hellsten A. On the Solid-Wall Boundary Condition of *ω* in the *k-ω*-Type Turbulence Models. *Report No B-50, Series B, Helsinki University of Technology, Finland*; 1998.

[21] Hellsten A. Some Improvements in Menter's k-ω SST Turbulence Model. *AIAA Paper 98-2554*; 1998.

[22] Wieghardt K. Tillmann W. Wieghardt, Flat Plate Flow. In *Computation of Turbulent Boundary Layers*, *Proc. of AFOSR-IFP Stanford Conference 1968*, *Stanford University;* 1969; pp. 98-123.

[23] Patel VC, Rodi W, Scheuerer G. Turbulence Models for Near-Wall and Low- Reynolds Number Flows: A

Review. *AIAA Journal*; 1985; **23**:1308-1319.
[24] Bardina JE, Huang PG, Coakley TJ. Turbulence Modeling Validation, Testing, and Development. *NASA TM-110446*; 1997.
[25] Heidegger NJ, Hall EJ, Delaney RA, Follow-on Low Noise Fan Aerodynamic Study. *NASA CR-1999-206599*; 1999.
[26] Driver DM, Johnston JP. Experimental Study of a Three-Dimensional Shear-Driven Turbulent Boundary Layer with Streamwise Adverse Pressure Gradient. *NASA TM 102211*; 1990.
[27] Rudy DH, Strikwerda JC. A Nonreflecting Outflow Boundary Condition for Subsonic Navier-Stokes Calculations" *J. Comp. Phys.* 1980; **36**:55-70.
[28] Dudek JC. Georgiadis NJ. Yoder DA. Calculation of Turbulent Subsonic Diffuser Flows Using NPARC Navier-Stokes Code. *AIAA Paper 96-0497*; 1996.
[29] Shih,T-H. Turbulence Modeling Developments at ICOMP. *AIAA Paper 98-3243*; 1998.
[30] Findlay M. An Experimental and Numerical Investigation of Inclined Jets in a Crossflow. *Ph. D. thesis, University of British Columbia, Canada*; 1998.
[31] Hassan I, Findlay M, Salcudean M, Gartshore I. Prediction of Film Cooling with Compound-Angle Injection Using Different Turbulence Models. *Proc. of CFD `98, CFD Society of Canada*; 1998; pp. x1-x6.
[32] Kim S-W, Benson TJ. Fluid Flow of a Row of Jets in Crossflow - A Numerical Study. *AIAA J.* 1993; **31**:806-811.
[33] Alvarez J, Jones WP, Seoud R. Predictions of Momentum and Scalar Fields in a Jet in Cross-Flow using First and Second Order Turbulence Closures. *AGARD-CP-534*; 1993; pp.24-1 - 24-10.
[34] Zhang X. Interaction Between a Turbulent Boundary Layer and Elliptic and Rectangular Jets. In *Engineering Turbulence Modelling and Experiments 2*, Rodi W and Martelli F (eds.); 1993; pp. 251-260.
[35] Barberopoulos AA, Garry KP. The Effect of Skewing on the Vorticity Produced by an Airjet Vortex Generator. *The Aeronautical J.* 1998; Paper No. 2275, pp. 171-177.
[36] Khan ZU. On the Dominant Vortex Created by a Pitched and Skewed Jet in Crossflow. *Ph. D. thesis, Stanford University*; 1999.

Acknowledgments

The financial support of National Research Council of Canada under contract no. 31184-8-8847/001/ST, and the assistance of Dr. T. Currie in setting up this contract are hereby gratefully acknowledged. Thanks are also due to Drs. I.S. Gartshore and M.J. Findlay for making their experimental data on the inclined-jet-in-crossflow available.